Journal of The Electrochemical Society, **166** (2) A364-A377 (2019)
0013-4651/2019/166(2)/A364/14/$38.00 © The Electrochemical Society

Understanding the Mechanism of Stress Mitigation in Selenium-Doped Germanium Electrodes

X. Wang,[1] C. O. Yenusah,[1] K. Tantratian,[1] M. L. Meyerson,[2] A. Guo,[2] C. Buddie Mullins,[2,*] L. Zhu,[3] and L. Chen[1,z]

[1]*Department of Mechanical Engineering, Mississippi State University, Mississippi State, Mississippi 39762, USA*
[2]*McKetta Department of Chemical Engineering, University of Texas at Austin, Austin, Texas 78712, USA*
[3]*Department of Mechanical and Energy Engineering, Indiana University-Purdue University Indianapolis, Indianapolis, Indiana 46202, USA*

This paper aims to investigate the mechanism of stress mitigation in micrometer (μm) sized Selenium (Se)-doped Germanium (Ge) electrode, which includes a self-forming inactive Li-Ge-Se network enveloping multiple nanometer-sized crystalline Ge (*c*-Ge) particles. Considering the electrode system contains multiply active particles, models based on single-particle are unable to fully understand elusive underpinning mechanism. Hence, a phase-field model is employed to investigate the effect of the Li-Ge-Se network on the particle-particle interaction, and the stress variation of the electrode upon lithiation. The amorphous Li-Ge-Se network provides an effective Li diffusion path for inter-particle diffusion, reducing stress difference between the surfaces of neighboring particles. Furthermore, the constraint between the adjacent particles induces a higher compressive stress at the reaction front impeding the mobile Li insertion during lithiation. Though small *c*-Ge nano-particle in the $Ge_{0.9}Se_{0.1}$ microparticle is lithiated quickly, the compressive stress is generated at its center for stress equilibrim causing more retardation effect. Meanwhile, the size difference between adjacent particles increases the principle and shear stresses in the inactive Li-Ge-Se, which could potentially lead to mechanical failure and debonding of the amorphous network. We believe that the results of this investigation can shed some light on the optimization design of electrodes.
 [DOI: 10.1149/2.1091902jes]

Manuscript submitted September 17, 2018; revised manuscript received January 14, 2019. Published February 1, 2019.

Li-ion batteries (LIBs) have become the major power source for portable devices and electric vehicles in recent decades. Innovation in LIBs technology is driven by the imperative demand for high-storage capacity, light weighting, and affordability.[1–7] The use of alloy-type anode materials is an attractive option due to their much higher storage capacity compared to graphite (372 mAh/g). An example is the broadly studied Si-based materials with low voltage and the high volumetric capacity (4200 mAh/g for $Li_{15}Si_4$).[2,5,8–10] In recent years, Ge-based anode materials have received lots of attention from academic and industrial entities due to their higher electrical conductivity compared to Si-based anode materials.[11,12] Besides, Ge-based anode materials show better mechanical performance than Si-based ones. Chan et al. investigated onset voltage for lithiation of the (100), (110), and (111) planes in both Si and Ge single crystal via combination of first principles calculations, electrochemical experiments, and Raman spectroscopy. Their results indicated that lithiation of Ge is independent of orientation, unlike Si.[13] Liang et al. concluded based on in situ TEM study that the weak anisotropy of the lithiation strain at the reaction front contributes to mechanically robust behavior of Ge nanoparticles.[14] They observed fracture free for particles with a large initial diameter, i.e., 620 nm, after multiple cycles.[14] The isotropic nature of lithiation contributes to this resistance to fracture,[14] compared to highly anisotropic lithiation found in *c*-Si electrodes.[15] Vlassak et al. found out Ge electrodes are more resilient to fracture than their Si counterparts via performing in-situ measurements of the stresses, stiffness, and fracture energy of *a*-Li_xGe thin-film electrodes during electrochemical cycling.[16] However, as an alloy-type material, Ge can undergo a high volume expansion (261%) during lithiation.[17] A major impediment to the use of alloy-type anode materials is the mechanical degradation (i.e., surface failure) of the electrodes in LIBs because of large swelling and shrinkage during charging/discharging cycles.[18–21] Mukherjee et al. deployed computational methods to study mechanical-electrochemical interaction in silicon-type high-capacity electrodes, and concluded that the majority of the microcracks evolve at or near the particle surface due to high volume expansion induced tension during lithiation.[22–24]

One of the proposed solutions to avoid mechanical degradation is the use of nano-structured alloy-type anode materials, which alleviates the electrode particle fracture because of the facile strain accommodation and short diffusion path for electron and Li-ion transport in the nanostructured electrodes.[25–29] However, site reaction during over-charging or fast-charging may lead to inhomogeneous Li dendritic growth on the electrode surface, which could cause a short circuit in the LIBs.[30] Also, an increase in the surface area of the material from the use of smaller particle size results in a large irreversible capacity loss because of the formation of solid electrolyte interphase (SEI).[31] Furthermore, nano-structured particles have low tap density and lead to lower energy density anodes, making scale up difficult.[3]

To improve the electrochemical performance of alloy-type LIBs, several design strategies have been applied to mitigate the chemo-mechanical degradation of the electrode materials. Surface coating is one of those strategies.[32,33–35] Such a coating layer acts as a multi-functional layer, suppressing the volumetric change upon lithiation therefore preventing cracking and pulverization of electrode materials. However the layer also impacts the chemical reaction kinetics and diffusion rate in the lithiated region by tuning the stress distribution inside the electrode.[32] If the layer increases compressive mean stress at reaction front, the compressive mean stress will contribute a negative driving force for lithiation, thus, slowing down further lithiation.[36,37] The stress induced self-limiting lithiation, or stress retardation effect, has been demonstrated by recent in-situ TEM studies: the migration of the reaction front in Si and Ge slowed down considerably as lithiation proceeded.[38–40] On the other hand, common surface coating methods such as alloying with metallic oxide are often time consuming or cost-intensive.[33–35] Recently, Mullins's group[41–43] proposed a self-forming active/inactive phase design of a micrometer (μm)-sized Se-doped Ge particles, where a network of active Ge inclusions amidst an amorphous Se-containing inactive phase is automatically formed during the initial lithiation cycle as shown in Fig. 1. Preliminary studies have shown that micrometer (μm)-sized Se-doped Ge particles vastly outperform un-doped Ge particles of similar size,[3] without surface fracture nor severe capacity fade for hundreds of cycles,[3,44] as compared in Figs. 1a–1c (pure *c*-Ge microparticles after charging/discharging) and Figs. 1d–1f ($Ge_{0.9}Se_{0.1}$ -based microparticles after charging/discharging). We investigated the effect of stress on the lithiation kinetics as shown in our previous work that the stress retardation effect is much less with a soft coating layer than with the hypothetical hard coating layer.[45] Therefore, for optimizing design of $Ge_{0.9}Se_{0.1}$-based LIBs, the fundamental understanding of the role of

*Electrochemical Society Member.
[z]E-mail: chen@me.msstate.edu

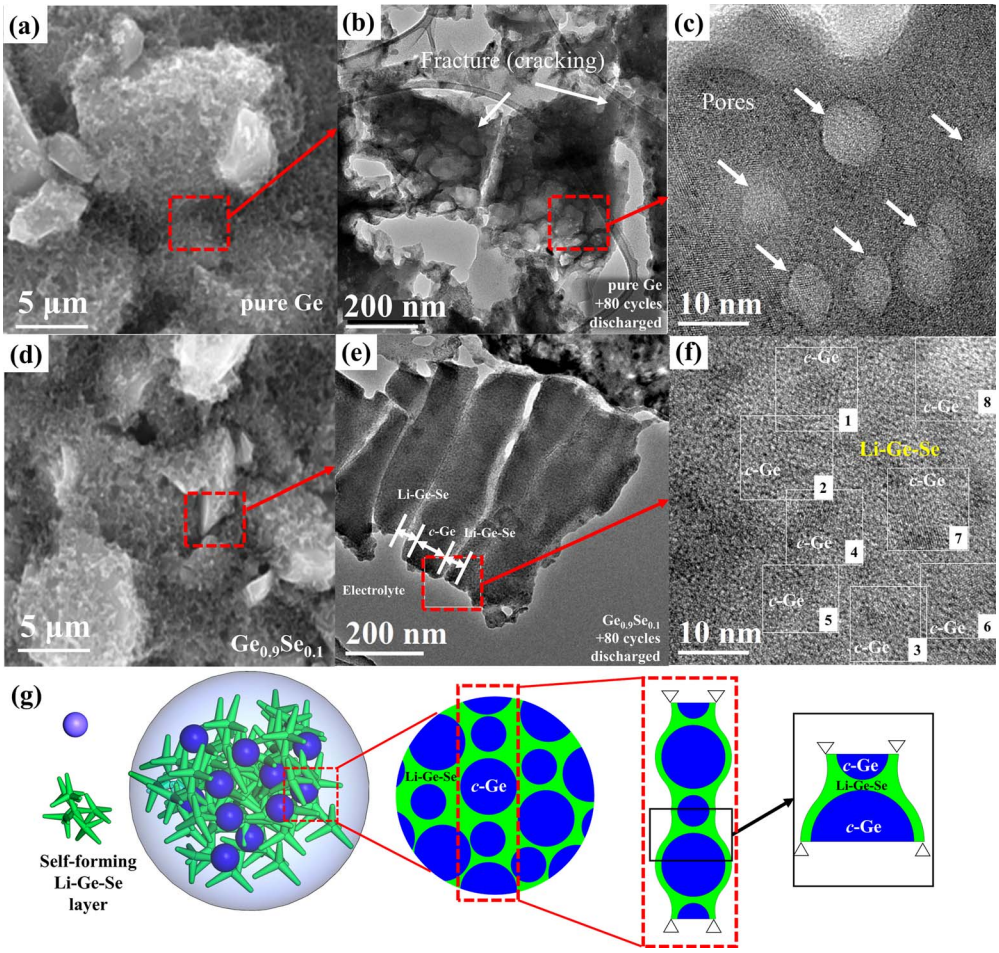

Figure 1. (a) TEM of cycled pure Ge particles from the pure Ge-based electrode. (b) The particle appears torn and fracture at the edges, (c) Nanometer-sized pores are observed throughout the interior of a micrometer-sized particle. (d) HR-TEM of an electrode particle from the $Ge_{0.9}Se_{0.1}$-based electrode. (e) Within the particle, there is no pore or cavity. (f) Higher magnification of a $Ge_{0.9}Se_{0.1}$ particle reviles several crystallite Ge regions (1 to 8) surrounded by an amorphous Li-Ge-Se inactive phase. (g) Schematic showing the micrometer-sized Se-doped Ge particles form a network of active Ge inclusions amidst an amorphous Se-containing inactive Li-Ge-Se phase, inspired by the experimental observations in (e)-(f).

the inactive phase in the stress mitigation of active electrode particles is necessary.

It had been widely accepted that the lithiation-induced stress plays an important role in the electrochemical processes.[46,47,21,48–58] Thus, numerous numerical models, i.e., chemo-mechanical models, have been developed to investigate how the lithiation-induced stresses change the kinetics of Li diffusion and interface reactions.[21,48–58] These chemo-mechanical models often treated the lithiation-induced stress as a diffusion-induced stress by considering Li diffusion in a solid-state electrode that results in the change of composition from its stoichiometric state. If the Li distribution is non-uniform, deviation from stoichiometry often causes a volume change which generates stresses.[59] The resulting stresses modulate the lithiation kinetics in lithiated electrodes.[38,60,61] Therefore, by developing a reaction-diffusion phase field model coupled with elasto-plastic deformation, a previous investigation of $Ge_{0.9}Se_{0.1}$-based electrode particles focusing on a single and isolated nanometer-sized electrode particle (*c*-Ge) enveloped by Li-Ge-Se coating has been conducted.[45] The soft Li–Ge–Se coating is found to reduce the compressive mean stress at the reaction front, thus alleviating the stress retardation effect on the lithiation kinetics. However, these results based on a single, isolated particle with idealized structure can only partially reveal the physical underpinnings of previously unexplained favorable chemical reaction, diffusion and fracture behavior of Se-doped Ge electrodes. Since the electrodes can be treated as a composite including active materials (usually consisted of multiple active particles, i.e., Si, Ge or graphite) and a conductive coating layer (i.e., Li-Ge-Se network in our study),[62] the electromechanical properties of the coating layer can greatly impact on the general performance of electrodes. Further, the particle-particle interaction can play an important role on regulating active particles' morphology and stress evolution during lithiation. Hence, studies based on single-particle are unable to fully understand elusive underpinning mechanism. Several research groups show that the maximum value of lithiation-induced stresses in the realistic particle is much higher than the prediction from the isolated, idealized models.[63,64] Concluding from previous chemomechanical simulations of electrode with multi-particles (i) The microstructure of electrode particles strongly impacts the stress generation (i.e., pressure from neighboring lithiated particles), Li diffusion/concentration (i.e., a low Li influx may result in diffusion-controlled lithiation), and mechanical failure. (ii) In a multi-particle system, the value of resulting stresses can be significantly higher than the one in single isolated particles. (iii) The mechanical properties of conductive coating layer, particularly the yield stress and elastic modulus, play important roles in determining the average stresses developed in the electrodes.[64–66] Hence, in order to understand the chemo-mechanical behaviors of $Ge_{0.9}Se_{0.1}$ based electrodes, it is necessary to study stress evolution and phase morphology among nanosized Ge particles enveloped by Li-Ge-Se network.

In this paper, we aim to investigate stress mitigation in the micrometer-sized $Ge_{0.9}Se_{0.1}$ electrode particle via the effect of *c*-Ge nanometer-sized sub-particle interaction in a network of

Li-Ge-Se. Here, we construct the 2D model inspired by experimental observations, as the network of inactive Li-Ge-Se phase enveloping nanometer-sized *c*-Ge particles,[3,42] as shown in Fig. 1g. Then, we employ a reaction-diffusion phase-field model[45] coupling elasto-plastic deformation to investigate the stress field evolution and the mechanical interaction in regulating the Li distribution and stress retardation of lithiation kinetics. First, we investigate particle-particle interactions by exploring the concurrent evolution of phases, morphologies and stress between two $Ge_{0.9}Se_{0.1}$-based particles with unequal size. Second, we study phase evolution and stress mitigation under the influence of Li-Ge-Se network in an image-based model by including many particles of randomly distributed sizes.

Modeling

Problem description.—Fig. 1 compares transmission electron microscopy (TEM) images of a pure Ge based electrode and a $Ge_{0.9}Se_{0.1}$-based electrode particles after 80 cycles of variable *C*-rate testing.[43] Fig. 1a reveals the micrometer (μm)-sized pure Ge particles. On further magnification, Fig. 1b reveals fracture and torn structure at the edges of a Ge particle caused by large deformation and anisotropic volume change during charging/discharging cycles. Also, the nano-pores that form in the Ge particle (Fig. 1c) indicates the large irreversible plastic deformation undergone by pure Ge electrode during cycling. Fig. 1d reveals the micrometer (μm)-sized $Ge_{0.9}Se_{0.1}$-based particles. On further magnification, the HR-TEM image, Fig. 1e, shows a fracture-free structure of a cycled $Ge_{0.9}Se_{0.1}$ particle. Fig. 1f reveals 10nm clusters of nanometer-sized *c*-Ge particles (numbered 1 to 8) enveloped by amorphous Li-Ge-Se network. The amorphous Li-Ge-Se network brings the superior electrochemical performance of the $Ge_{0.9}Se_{0.1}$ electrode in cycling stability and capacity over un-doped Ge particles.[43] However, the formation mechanism is not our focus in this study, rather, the tempo-spatial morphology, phase change between neighboring particles, and stress evolution of the *c*-Ge particles surrounded by the Li-Ge-Se network are our main concerns. For simplicity, we illustrate the mechanism by taking the lithiation of two spherical *c*-Ge particle with different radii as schematically shown in Fig. 1g.

Unlike the pure *c*-Ge particles, Se-doped Ge particles are enveloped by a self-forming inactive Li-Ge-Se network with high Li capacity and diffusivity, which does not participate in chemical reaction. Hereby, we define two states of Li atom to describe the Li diffusion and chemical reaction, as mobile Li and immobilized Li, respectively (see details in Phase-field model section). Meanwhile, the lithiation arises from three kinetic processes in series that are (i) the redox reaction (a charge transfer reaction) at the electrolyte/Li-Ge-Se interface, (ii) the diffusion of the mobile Li through the Li–Ge–Se layer and the *a*-$Li_{x0}Ge$ phase, and (iii) the chemical reaction (a bulk reaction) at the *a*-$Li_{x0}Ge$/*c*-Ge interface where the mobile Li is changed to the immobilized status (See details in Appendix and Figure A2). Therefore, the local distribution of mobile Li concentration determines the lithiation reaction kinetic (reaction- or diffusion-controlled), as we have discussed in the previous work.[45] The inactive Li-Ge-Se network as a high conductive surface film has a high Li atom diffusivity, which can transport a large amount of mobile Li to the nanometer sized sub-particles during lithiation. For the *c*-Ge nanometer sized sub-particles located close to the outer surface of $Ge_{0.9}Se_{0.1}$-based particles (electrode/electrolyte interface) may have sufficient mobile Li during lithiation, the reaction-control kinetic will dominate the lithiation reaction. However, for the *c*-Ge clusters located away from the outer surface, the lithiation kinetic can be diffusion-control once the local distribution of mobile Li is not enough. Such difference in lithiation kinetics can directly lead to inhomogeneous lithiation, and, therefore, dramatical stress variations, which thereby results in the loss of electrical contact and limits the life cycle of LIBs. On the other hand, when the sizes are unequal between adjacent enveloped *c*-Ge particles, the geometrical effects play important role leading to different lithiation levels and lithiation-induced stress. The influence of such difference can be reflected on the Li distribution near adjacent particles (i.e., lower Li distribution). Hence, in addition to the pervious investigation on an isolated *c*-Ge enveloped by Li-Ge-Se layer, it is important to study the role of the inactive Li-Ge-Se network in the evolution of phase, morphology and stress in the active/inactive phase electrode particles during the lithiation process in three aspects: 1) Comparison of electrochemical performance of contact particles verse enveloped particle; 2) The influence of size difference on particle-particle interaction; 3) Image based cluster of *c*-Ge particle interaction for a more practical investigation.

Stress equilibrium.—The local stress relaxation is much faster than the long-range Li diffusion and chemical reaction, thus, the stress equilibrium for all material points holds at any time, i.e.

$$\nabla \cdot \boldsymbol{\sigma} = 0 \,\text{on}\, V \qquad [1]$$

Further, regarding the mechanics boundary conditions, we assume the outer surface of the inactive coating layer $\Gamma^d_{\text{Li-Ge-Se}}$ is traction free

$$-\mathbf{n} \cdot \boldsymbol{\sigma} = 0 \quad \text{on}\ \Gamma^d_{\text{Li-Ge-Se}} \qquad [2]$$

where $\mathbf{n}$ is the outward normal at the outer surface $\Gamma^d_{\text{Li-Ge-Se}}$. The stress is a function of the deformation gradient $\mathbf{F}$, that is defined as $\mathbf{F} = \mathbf{F}^e\mathbf{F}^*$, $\mathbf{F}^* = \mathbf{F}^c\mathbf{F}^p$, where $\mathbf{F}^c$ means the chemically-induced deformation gradient for the compositional inhomogeneity, $\mathbf{F}^p$ is the plastic deformation gradient, and $\mathbf{F}^e$ is the elastic deformation gradient. An accumulation of an inelastic deformation $\mathbf{F}^*$ followed by an elastic deformation $\mathbf{F}^e$ can be used to describe the total deformation. We name the state after inelastic deformation $\mathbf{F}^*$ as the intermediate state.

Phase-field model.—Coupled with elasto-plastic deformation, the phase-field model (PFM) integrating chemical reaction, Li diffusion, and interfacial effects has been developed in previous work, and was applied to capture the reaction and/or diffusion lithiation kinetics.[45] In brevity, based on the bulk chemical reaction, x_0Li+*c*-Ge → *a*-$Li_{x0}Ge$, at the *a*-$Li_{x0}Ge$/*c*-Ge phase boundary within the electrode, is specifically considered as a phase transformation with an abundant availability of *c*-Ge. As the number of moles of Li in the alloyed *a*-$Li_{x0}Ge$ phase and we use $x_0 = 3.75$ in this study based on the published experimental results.[42] To simulate the concurrent Li diffusion and chemical reaction, two phase-field parameters will be defined corresponding to the states of Li during the lithiation process: 1) we define the mobile Li (as unreacted Li atoms) distribution in the phases via the normalized concentration field (molar fraction), c_{Li}. 2) a continuous phase-field variable, ξ, is introduced to describe the immobilized Li state (reacted Li), and applied to separate *a*-$Li_{x0}Ge$ and *c*-Ge during the phase transformation. Besides, the lithiation-induced chemical deformation is isotropic resulting from both the Li diffusion and the reversible chemical reaction. Thus, with above parameters, the chemically-induced deformation gradient $\mathbf{F}^c$ can be expressed as, $\mathbf{F}^c = \beta_1\ \xi\ \mathbf{I} + \beta_2\ c_{\text{Li}}\ \mathbf{I}$, in which, β_1 and β_2 are the expansion coefficients corresponding to the deformation donated by the immobilized and the mobile Li, respectively, and $\mathbf{I}$ is the identity tensor.

With the above two phase-field parameters, we define the total free energy functional of the heterogeneous material expressed as[45,67,68]

$$G = \int_V f dV = \int_V \left[f_{ch}(\xi) + f_{mobile}(c_{\text{Li}}) + \frac{\kappa_\xi(\nabla\xi)^2}{2} + \frac{\kappa_c(\nabla c_{\text{Li}})^2}{2} + f_\sigma(\mathbf{F}, \xi, c_{\text{Li}}) \right] dV \qquad [3]$$

where the terms $\kappa_\xi(\nabla\xi)^2/2$ and $\kappa_c(\nabla c_{Li})^2/2$ are the gradient energy densities associated with the interfacial energy. $f_{ch}(\xi)$ corresponds to the local chemical free energy density, reads $f_{ch}(\xi) = g(\xi) + h(\xi)\eta$, where the constant term $\eta = -0.5$eV in the assumption represents a driving force combining the electrostatic effect and the standard potential difference between reactants and products ($\Delta\mu = \mu_{LiGe} - \mu_{Ge}$), in which the entropic driving force over the mobile Li is negligible. $g(\xi) = W\xi^2(1-\xi)^2$ is a double-well function describing the two equilibrium states separating the reactant ($\xi = 0$) and resultant

($\xi = 1$) phases mathematically and *W/16* is the artificial energy barrier height. $h(\xi) = \xi^3(6\xi^2 - 15\xi + 10)$ is an interpolating function corresponding to the state of charge which is interpolated between the *c*-Ge, (as $h(0) = 0$) and *a*-$Li_{x0}Ge$ (as $h(1) = 1$) phases.[69–71] Here, neither the double-well energy function nor the energy barrier carries any physical significance. They are introduced, in conjunction with the gradient energy $\kappa_\xi(\nabla\xi)^2/2$, just to form interface between the unreacted and resultant phases. Meanwhile, W and κ_ξ determine a scale length, as $\sqrt{\kappa_\xi/W}$, which characteristic thickness of the phase boundary. i.e. reaction front. However, in this work, we only apply a particular choice for both W and κ_ξ, due to the lack of the direct measurement for the actual thickness of the reaction front. Once the thickness of reaction front is measured from experiments, it can be directly applied to the future simulation.

$f_{mobile}(c_{\mathrm{Li}})$ is the free energy density of the mobile Li interacting with host matrices. $f_\sigma(\mathbf{F}, \xi, c_{\mathrm{Li}})$ is the elastic energy density induced by the inhomogeneous lithiation defined in the Lagrangian description (initial configuration). (See details in Appendix).

The phase-field evolves driving by

$$\frac{\partial \xi}{\partial t} = -M_\xi \frac{\delta G}{\delta \xi} = -M_\xi \left(g'(\xi) + h'(\xi)\,\eta + \kappa_\xi \nabla^2 \xi + \mu_\sigma^\xi\right) \qquad [4]$$

where M_ξ is a function controlling the rate of chemical reaction. We assume that M_ξ is proportional to the concentration of the mobile Li, expressed as $M_\xi = L_\eta c_{Li}$, of which L_η is the non-negative constant.[72] It is noted that at the stress-free state with η is unchanged, a higher mobile Li concentration, c_{Li}, increases the rate of chemical reaction, whereas a lower c_{Li} indicates a slower lithiation process. The stress driving force, μ_σ^ξ corresponding to the resulting stresses caused by the immobilized Li. (see details in Appendix).

The mobile Li diffusion in the host matrices is driven by

$$\frac{\partial c_{\mathrm{Li}}}{\partial t} = -\nabla \cdot \left(-D_{\mathrm{Li}}^{\mathrm{eff}} \nabla c_{\mathrm{Li}}\right) - \frac{x_0}{x_{\max}} \frac{\partial \xi}{\partial t} \qquad [5]$$

where the last term $\frac{x_0}{x_{\max}} \frac{\partial \xi}{\partial t}$ responses to the accumulation/consuming of the mobile Li due to lithiation reaction. $D_{\mathrm{Li}}^{\mathrm{eff}}$ is the effective diffusion coefficient: 1) $D_{\mathrm{Li}}^{\mathrm{eff}} = D_{\mathrm{Li}}^{\mathrm{LiGe}} h(\xi) + D_{\mathrm{Li}}^{\mathrm{Ge}}(1 - h(\xi))$, in the active lithiated Ge material ($D_{\mathrm{Li}}^{\mathrm{LiGe}}$ and $D_{\mathrm{Li}}^{\mathrm{Ge}}$ are the mobile Li diffusion coefficients in the lithiated Ge and unlithiated Ge respectively); 2) $D_{\mathrm{Li}}^{\mathrm{eff}} = D_{\mathrm{Li}}^{\mathrm{LiSe}}$, in the inactive Li-Ge-Se layer. (see details in Appendix). We had validated our model in our previous work[45] that the present PFM can reproduce the reaction-diffusion kinetics and the stress evolutions were well calibrated with experimental observations.

Parameters

COMSOL (version 5.2), a commercial software package was used to solve the PFM coupled with the constitutive equations for elasto-plastic deformation, using a FEM-based numerical scheme. The FEM-based approach can more efficiently integrate the phase-field and mechanics equations than the commonly used spectral method. Especially, under various initial and boundary conditions, it is suitable to solve the problems with elasto-plastic deformation and finite-sized geometry of an arbitrary shape.

The unlithiated Ge is considered as the pure Ge modeled as an isotropic and elastic material, with Young's modulus of 130 GPa and Poisson's ratio of 0.26.[73–75] An isotropic elasto-plastic model with a linear hardening law is adopted to describe the constitutive behavior of amorphous Li-Ge-Se and $Li_{x0}Ge$ phase upon lithiation. Currently, the elastic properties for both amorphous phases are unavailable, so the properties of a very similar alloy material (i.e. Li-Se-Ga) are adopted with the Young's modulus and Poisson's ration varying from 16 GPa to 24 GPa and from 0.24 to 0.26,[73] respectively. The elastic properties across the diffuse Ge/$Li_{x0}Ge$ interface vary linearly between the pure Ge and $Li_{x0}Ge$'s depending on the Li concentration. However, the materials properties of amorphous Li-Ge-Se and $Li_{x0}Ge$ in the plastic region are unavailable. Hereby, we use typical values for the yield strength $\sigma_{y0} = 1.2$ GPa, and the hardening modulus $H = 2.0$ GPa, which provide a reasonable fit to recent experiments.[42]

The diffusion expansion coefficient and the reaction expansion coefficient are $\beta_1 = \beta_2 = 0.5326$, both of which yield an experimentally observed volume increase of 261% in the fully lithiated phase. And the Li diffusion coefficients in pure Ge particle, $D_{\mathrm{Li}}^{\mathrm{Ge}}$, is obtained by the empirical equation as following:[32,76,77] $D_{\mathrm{Li}}^{\mathrm{Ge}} = D_0 \exp[-Q/RT]$ where $D_0 = 2.5 \times 10^{-8}\ \mathrm{m^2 \cdot s^{-1}}$ is the constant prefactor and $Q = 11800\ \mathrm{cal \cdot mol^{-1}}$ is the activation energy. Thus, we have $D_{\mathrm{Li}}^{\mathrm{Ge}} \approx 5.9 \times 10^{-17} \mathrm{m^2 \cdot s^{-1}}$, which is well consistent with the experimentally measured one by the potentiostatic intermittent titration technique (PITT) reported in Ref. 42.

In the present PFM, all the equations are solved in a dimensionless form. Both moduli and stresses are normalized by $E_0 = 1$ GPa that has been estimated as follows. The initial radius of nanometer-sized Ge particle is $A_l = 20$ nm and $A_s = 10$ nm for large and small particles respectively, and the thickness of Li-Ge-Se layer is given as $0.2A_l$ based on the experimental observation. The length parameters are normalized by $A_o = 10$ nm, yielding a normalized radius of unity. Besides, the characteristic time step Δt for lithiation evolution is taken

Table I. Phase-field simulation parameters and their normalized values.

	Real value		Normalized value	
Parameter	Symbol	Value	Symbol	Value
Reaction constant.	L_η	$5 \times 10^{-2}\ \mathrm{s^{-1}}$	$\tilde{L}_\eta = L_\eta \times \Delta t_0$	0.1
Gradient energy coeff.	κ	$5 \times 10^{-9}\ \mathrm{J \cdot m^{-1}}$	$\tilde{\kappa} = \kappa/(E_0 \times A_0{}^2)$	0.0001
Barrier height	W	$1.6 \times 10^{-8}\ \mathrm{J \cdot m^{-3}}$	$\tilde{W} = W/E_0$	16
Particle Radius (large)	A_l	20 nm	$\tilde{A} = A/A_0$	2.0
Particle Radius (small)	A_s	10 nm	$\tilde{A} = A/A_0$	1.0
Time step	Δt	0.002 s	$\Delta\tilde{t} = \Delta t/\Delta t_0$	0.001
Elastic Modulus of Ge	E_{Ge}	130 GPa	$\tilde{E}_{\mathrm{Ge}} = E_{\mathrm{Ge}}/E_0$	130
Elastic Modulus of $Li_{x0}Ge$	E_{LiGe}	30 GPa	$\tilde{E}_{\mathrm{LiGe}} = E_{\mathrm{LiGe}}/E_0$	30
Elastic Modulus of Li-Ge-Se	E_{LiSe}	16∼24 GPa	$\tilde{E}_{\mathrm{LiSe}} = E_{\mathrm{LiSe}}/E_0$	16∼24
Diffusion coeff. of Ge	$D_{\mathrm{Li}}^{\mathrm{Ge}}$	$5.9 \times 10^{-17}\ \mathrm{m^2 \cdot s^{-1}}$	$\tilde{D}_{\mathrm{Li}}^{\mathrm{Ge}} = D_{\mathrm{Li}}^{\mathrm{Ge}} \times \Delta t_0 \times A_0{}^{-2}$	0.03
Diffusion coeff. of $Li_{x0}Ge$	$D_{\mathrm{Li}}^{\mathrm{LiGe}}$	$8.5 \times 10^{-15}\ \mathrm{m^2 \cdot s^{-1}}$	$\tilde{D}_{\mathrm{Li}}^{\mathrm{LiGe}} = D_{\mathrm{Li}}^{\mathrm{LiGe}} \times \Delta t_0 \times A_0{}^{-2}$	0.425
Diffusion coeff. of Li-Ge-Se	$D_{\mathrm{Li}}^{\mathrm{LiSe}}$	$8.5 \times 10^{-14}\ \mathrm{m^2 \cdot s^{-1}}$	$\tilde{D}_{\mathrm{Li}}^{\mathrm{LiSe}} = D_{\mathrm{Li}}^{\mathrm{LiSe}} \times \Delta t_0 \times A_0{}^{-2}$	4.25
Yield Strength	σ_{y0}	1.2 GPa	$\tilde{\sigma}_y = \sigma_{y0}/E_0$	1.2
Strain Hardness	H	2 GPa	$\tilde{H} = H/E_0$	2

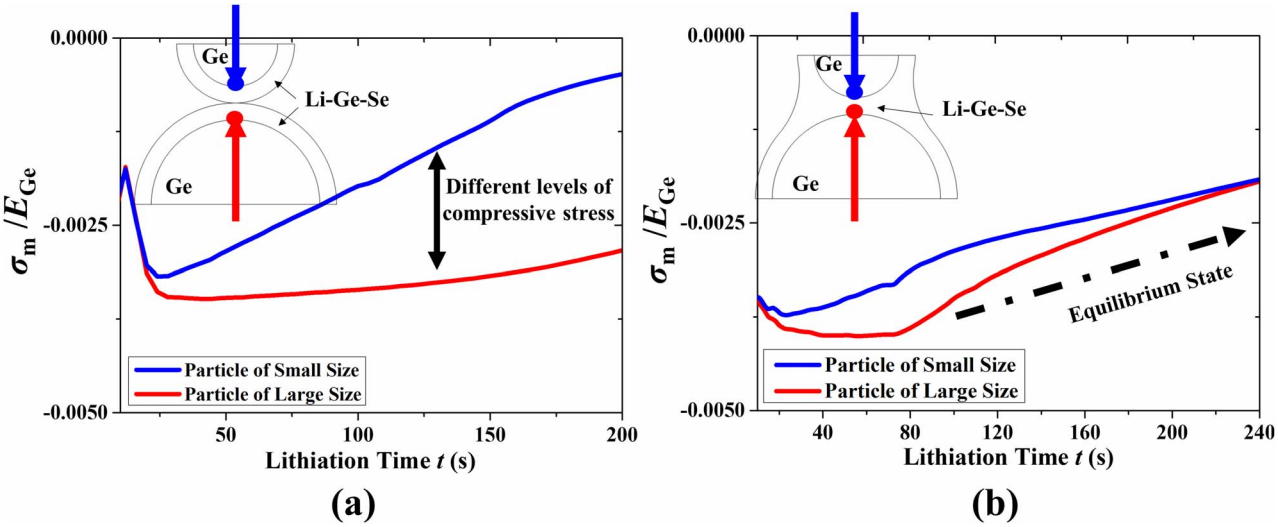

Figure 2. The variations of the lithiation-induced surface compressive mean stress, σ_m, in large and small particles with respect to lithiation time for (a) contact structure and (b) connective structure, respectively.

as 0.002 s. The physical parameters and their normalized value are summarized in Table I. Notice that the constant L_η and the electrostatic driving force ($\eta = -0.5$ eV) are kept fixed in this study.

Results and Discussion

Comparison between network structure and hypothetical contact structure of Li-Ge-Se phase.—Some researches focused on as an active particle enveloped by a protective and inactive binder to prevent mechanical degradation of active phase.[78,79] However, the network structure of inactive phase can be more effective in protecting particles from fracture and degradations. In this section, we make a comparison between a hypothetical contact structure and the network structure of Li-Ge-Se layer. In the contact structure configuration, each *c*-Ge particle is coated with a layer of Li-Ge-Se. Initial, the particles are isolated, and contact is made due to swelling from lithiation (shown in Fig. 2a). The network structure refers to the configuration of c-Ge particles are evenly enveloped with a Li-Ge-Se phase (Fig. 2b). For the boundary conditions, two phase-field order parameters are defined accordingly as two boundary conditions to solve two partial differential Equations: 1) $c_{Li} = \hat{c}_\beta$on $\Gamma^d_{Li-Ge-Se}$, which $\Gamma^d_{Li-Ge-Se}$ is the outer surface of the inactive Li-Ge-Se coating layer. 2) $\xi = 1$ and $c_{Li} \leq 0.15$ on Γ^d_{Ge}, which Γ^d_{Ge} corresponds to the interface between the active Ge particle and the inactive Li-Ge-Se coating layer. Further, for other mechanics boundary conditions, we assume the outer surface of the inactive coating network or layer $\Gamma^d_{Li-Ge-Se}$ is traction free, i.e., $-\mathbf{n} \cdot \boldsymbol{\sigma} = 0$ on $\Gamma^d_{Li-Ge-Se}$, accounting for the role of Li-Ge-Se coating network or layer in buffering volumetric expansion, where $\mathbf{n}$ is the outward normal at the outer surface $\Gamma^d_{Li-Ge-Se}$.

In experimental observations, the mobile Li was observed to quickly cover the outer surface of the Li-Ge-Se coating layer due to the high Li diffusivity in the liquid electrolyte.[21,80,81] Hereby, we prescribe three Dirichlet boundary conditions: i) a saturated normalized mobile Li concentration of $\hat{c}_\beta = 1$, corresponding to enough Li on the Li-Ge-Se outer surface throughout the lithiation process is assumed; ii) a Li-rich phase of $\xi = 1$, which indicates the lithiation reaction starts from the interface between the active Ge particle and the inactive Li-Ge-Se coating layer to the inside of Ge particle is prescribed; iii) the maximum or saturated concentration of the mobile Li on the boundary between the electrode and the Li-Ge-Se layer due to the capability of carrying Li atoms of lithiated Ge: $c_{Li} \leq 0.15$ or $c^{max}_{Li} = 0.15$.[45]

Fig. 2 shows the variation of surface mean stress at adjacent surfaces in both particles with respect to lithiation time for the contact structure and the network structure (given in Figs. 2a–2b, respectively). In Fig. 2a, after 25s of lithiation, the mean stress difference between the adjacent surfaces in both particles increases over time. However, in the network structure (shown in Fig. 2b), the stress difference between the adjacent surfaces in both particles increases from 10s to 80s during lithiation but decreases as lithiation proceeds, reaching an equilibrium state at 220s. The comparison reveals that the Li-Ge-Se network can provide even stress distribution near adjacent surfaces between neighboring particles.

The Li-Ge-Se network with the high Li diffusivity provides more diffusion paths for inter-particle diffusion than the hypothetical contact structure, which brings even stress distribution between the adjacent surfaces of neighboring particles upon lithiation. In general, the inter-particle diffusion happens when a chemical potential difference, given as $\Delta\mu_\sigma = |\mu^L_\sigma - \mu^S_\sigma|$, induced by the different stress levels at adjacent surfaces is greater than zero. $\Delta\mu_\sigma$ drives the inter-particle diffusion, pushing the mobile Li from the large particle to the smaller one near the contact region. Consequently, the mobile Li concentration, c_{Li}, in the large particle is diluted, generating a local negative driving force which drives the delithiation in the large particle but leads to instantaneous lithiation in the smaller one. As the inter-particle diffusion continues, it impacts the stress variation in both particles until the two particles reach an isopotential, i.e. $\Delta\mu_\sigma = 0$ (inter-particle diffusion stops), the lithiation resumes as a-$Li_{x0}Ge$ phase grows, resulting in $\Delta\mu_\sigma > 0$, which drives the inter-particle diffusion.[65]

In this study, however, the direct observation of lithiation/delithation is impossible due to the mesh density, time steps and computational cost. Instead, we use (see Fig. 3) the reaction driving force, $\partial\xi/\partial t$, at different times to show the inter-particle diffusion. In Fig. 3, the white arrow indicates the direction of reaction driving force, when it points inward it indicates a positive driving force and a tendency for lithiation. Conversely, pointing outward, it indicates a negative driving force and a tendency for delithiation. The size of each arrow indicates the magnitude of the reaction driving force. In Fig. 3a, large negative driving force is prevalent in the large particle showing a tendency of delithiation, corresponding to Fig. 2b, that during the initial stage of lithiation a higher compressive stress builds-up at the surface of the large particle. At the same moment, the smaller particle is dominated by positive driving force, as the inward pointing arrows indicate (Fig. 3a). As lithiation proceeds, (see Figs. 3b–3d) the magnitude of the driving force decreases as the compressive stresses on both particles surface equilibrates. The random distribution of arrows' direction is noticeable in Fig. 3 due to the mesh density and mobile Li diffusion causing uneven lithiation in the model. Therefore, when

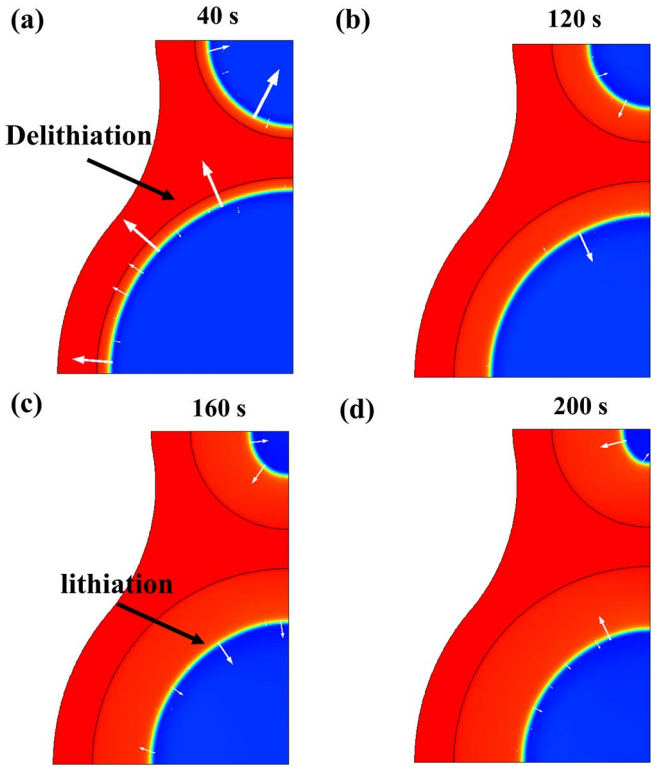

Figure 3. Comparison of the magnitude and direction of the reaction driving force at different time: (a) $t = 40$ s, (b) 120s, (c) 200s, and (d) 240s. The white arrow represents the direction and its size corresponds to the magnitude of the reaction driving force.

neighboring particles are in different sizes, the network structure of Li-Ge-Se can evenly redistribute the compressive stress at adjacent surfaces of neighboring particles.

Particle-particle interaction between two neighboring nanometer sized particles.—Previous works usually assume[82] that, regardless of the electrode particle's position, each particle has been evenly merged in the electrolyte, so that the lithiation of each particle is simultaneous. However, due to finite Li diffusivity in the Li-Ge-Se network, the nanometer sized sub-particles near the outer surface of micrometer sized electrode particle start lithiation earlier than those located far away from the outer surface. Fig. 4 shows the TEM image of a $Ge_{0.9}Se_{0.1}$-based electrode during lithiation. The mobile Li diffusion process that occurs in the amorphous Li-Ge-Se network can be expressed as: (1) redox reaction (a charge transfer reaction) at the electrolyte/Li-Ge-Se interface, (2) diffusion of mobile Li through the Li-Ge-Se layer. Hence, inspired by the actual lithiation process, we change the mobile Li influx boundary condition from the outer surface of the Li-Ge-Se to the small particle simulating the Li diffusion inside of the network, assuming the large particle to be located in the interior of the Ge cluster. When a mobile Li atom entering the outer surface, it has to travel along the Li-Ge-Se network to reach each particle. Fig. 4b shows the axisymmetric finite element model for the particles. R_c, R_f and T_{se} are the radius of particles in contact direction, the radius of particles in free direction, and thickness of the inactive Li-Ge-Se layer, respectively. The red arrows indicate the mobile Li influx, where $c_{Li} = \hat{c}_\beta$. Notice that rest of the boundary conditions applied in this case are the same as in Section Comparison between network structure and hypothetical contact structure of Li-Ge-Se phase.

Fig. 5a shows the variation of the mean stress, σ_m (normalized by the Young's modulus of pure Ge), between two particles at different lithiation times (18s, 120s and 240s). Notice that we show the stress evolution align with the representative lithiation depths, which is specified by the position of reaction front in the reference configuration. Hence, the deformation due to lithiation is neglected in the plots. The mechanical confinement in contact direction results in a higher compressive mean stress at the reaction front in both particles along the R_c direction than the one along R_f. The lithiation thickness of each particle has been normalized by the radius of large particle (a_f^l for the large particle and a_f^s for the smaller particle, respectively) for comparison.

For the large particle, Fig. 5b compares the radial distributions of mean stress along the free direction, R_f^l, and along the direction of R_c^l. The compressive mean stress at reaction front along the contact direction is higher than along the free direction due to inter-particle contact. Similarly, we obtain the radial distribution of mean stress in the small particle as shown in Fig. 5c, in which a higher compression at the reaction front is observed along the contact direction than the free direction. Reason being that, at the same time, the small particle has a higher percentage of lithiated phase than the large particle. Also, the lithiation kinetic in the small particle is completely reaction-control as shown in Fig. 6a, which results in a faster lithiation and a shorter relaxation time for dissipation of compressive stress. Meanwhile, during lithiation in the large particle, the lithiation kinetic is both reaction and diffusion control. In the earlier stage, the lithiation kinetic is reaction-controlled but then transits to diffusion-controlled as the phase boundary moves deeper. This transition slows down the lithiation process resulting in a longer relaxation time for the dissipation of accumulated stress. Notice that the compressive mean stress can lead to a negative driving force for the chemical reaction.

Furthermore, we compare the mobile Li distribution in two cases: 1) with the stress effect and 2) without any stress effect. Given in Figs. 6a–6b, the stress retardation effect leads to slower phase evolution near adjacent surface of both particles (consistent with the mean stress distribution in Fig. 5).

To exam the stress retardation effect due to the mechanical confinement of the particles by the Li-Ge-Se coating, we check the total Li profile for both particles. Although the particles do not make direct contact because of the Li-Ge-Se buffer, the large compressive stress generated by the contact effect of both particle (see Fig. 5a) plays an important role in the Li profiles when the stress effect is considered (as shown in Fig. 6a). Fig. 6c and Fig. 6e shows the Li profiles along the contact radial direction at different lithiation times (120s and 240s). The solid and dash lines represent the Li profiles when the stress effect on Li diffusion is ignored and when it is accounted for, respectively. In both plots, with the mechanical confinement from the Li-Ge-Se phase, the Li insertion into the particles is suppressed due to the compressive stress. As lithiation proceeds, the suppressed effect is more obvious, especially in the smaller particle as shown in

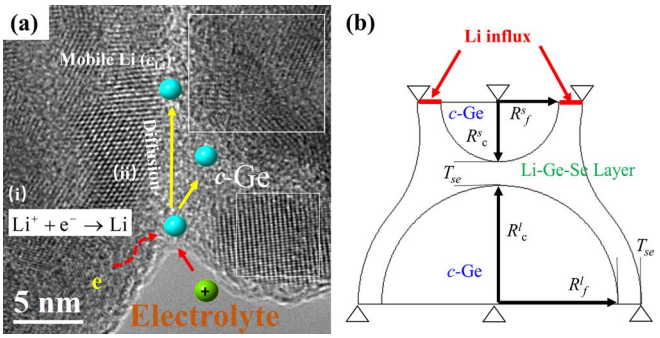

Figure 4. (a) Schematic shows the diffusion process of mobile Li in Li-Ge-Se network, (i) redox reaction (a charge transfer reaction) at the electrolyte/Li–Ge–Se interface (ii) diffusion of mobile Li through the inactive Li–Ge–Se and a-$Li_{x0}Ge$ phase. (b)Schematic drawing of aggregating anode aligning in one-dimension and the axisymmetric finite element model for the network structure particles. R_c, R_f and T_{se} are the radius of particles in contact direction, the radius of particles in free direction, and thickness of inactive Li-Ge-Se, respectively. The red arrows indicate the Li influx.

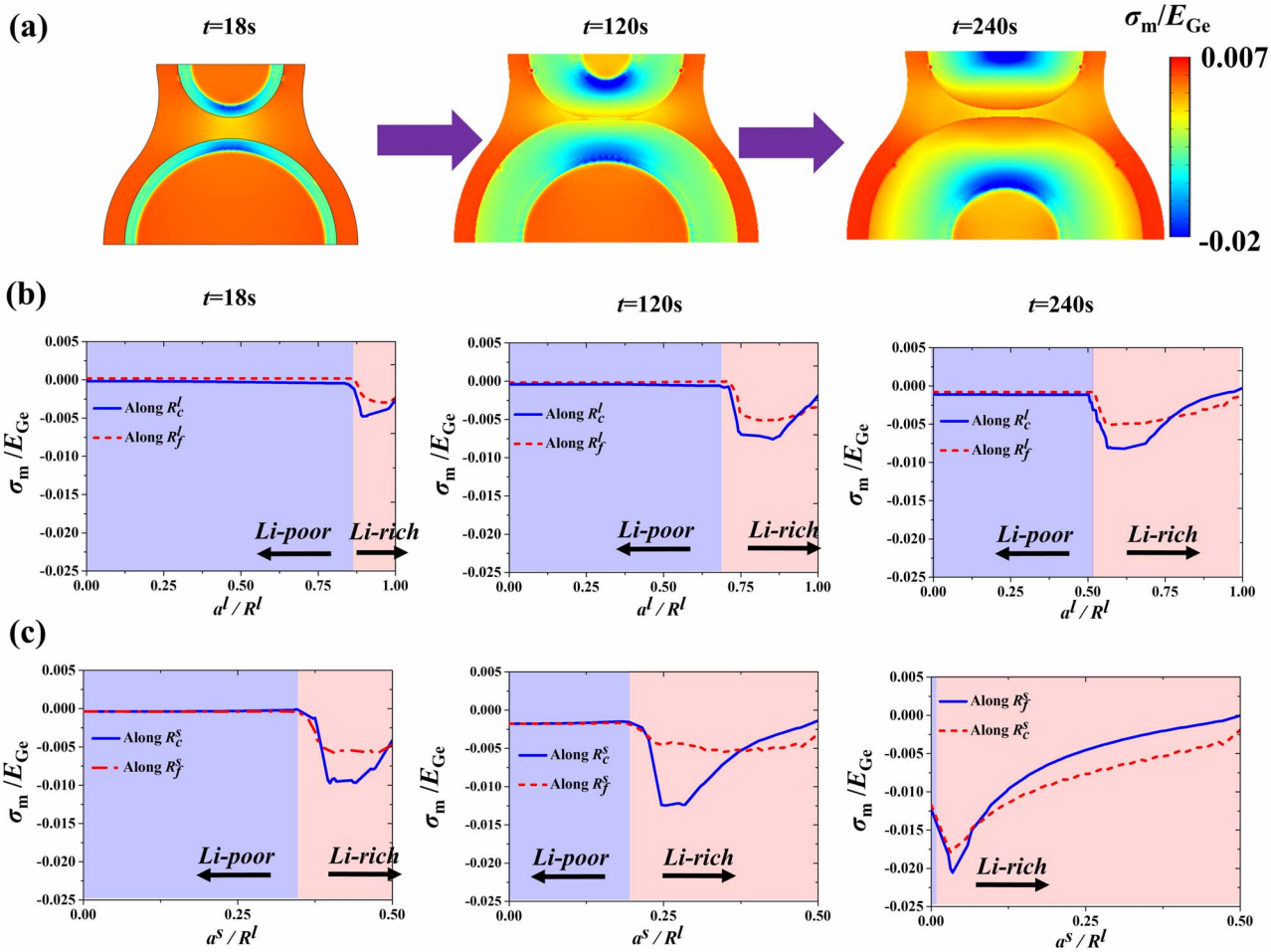

Figure 5. (a) Contour plots showing the distribution of mean stress (σ_m) normalized by the Young's modulus of pure Ge (E_{Ge}) at different lithiation times: t = 18s, 120s and 240s. (b) Comparison of radial distribution of the mean stress (σ_m) at different lithiation times: t = 18s, 120s and 240s along the free radius (R_f^l) and along the contact radius (R_c^l) for the large particle. (c) Comparison of radial distribution of the mean stress (σ_m) at different lithiation times: t = 18s, 120s and 240s along the free radius (R_f^s) and along the contact radius (R_c^s) for the smaller particle.

Fig. 6e. At 240s, the smaller particle is almost fully lithiated, but mechanical confinement attributed by the Li-Ge-Se layer causes a 20% less utilization. Fig. 6d and Fig. 6f compare the Li distribution along the free and contact radial direction for both particles. The contact effect from both particles results in large compressive stress at the reaction front, which can cause a large stress retardation effect. It means that the capacity is more affected in the smaller particle than the lager one.

Particle-particle interaction in micrometer sized $Ge_{0.9}Se_{0.1}$ electrode particle.—One micrometer sized $Ge_{0.9}Se_{0.1}$-based electrode particle usually contains multiple nanometer sized sub-particles (*c*-Ge). Due to the size difference and the finite Li diffusivity in Li-Ge-Se, the interaction among these nanometer sized particles can cause debonding or fracture failure in Li-Ge-Se network upon lithiation. Though the fracture may be eliminated at the surface of active nanometer sized *c*-Ge sub-particles, the debonding or fracture of protective Li-Ge-Se phase can still cause problems, i.e., reduced diffuse path leading to uneven lithiation. Therefore, in this section, we use an image-based model to investigation particle-particle interaction in micrometer-sized $Ge_{0.9}Se_{0.1}$ electrode particle.

As shown in Fig. 7a, the experimental TEM image tells no fracture in $Ge_{0.9}Se_{0.1}$-based electrode particles before lithiation. However, after 80 cycles of charging/discharging, we can see that the fracture failure of Li-Ge-Se network (marked with yellow arrows) located between adjacent micrometer-sized particles (see Fig. 7b). Also, the fracture can be found inside of the micrometer -sized particle by amplifying the chosen region of the electrode (see Fig. 7c). By further amplifying the selected region in Fig. 7c, we obtain the HR-TEM image of the active material, *c*-Ge particle, surrounded by an amorphous Li-Ge-Se phase (see Fig. 7d). From this, we constructed a corresponding 2D model, as given in Fig. 7e, the *c*-Ge particles (blue) are buffered by the Li-Ge-Se network (Green) as shown in Fig. 7f. The radii of the *c*-Ge particles are varied from 5 nm to 30 nm. The boundary conditions are given as following: $c_{Li} = \hat{c}_{\beta} = 1$on $\Gamma^d_{\text{electrode}}$, where $\Gamma^d_{\text{electrode}}$ is the outer surface of the particle cluster. $\xi = 1$ and $c_{Li} \leq 0.15$ on Γ^d_{Ge}, which Γ^d_{Ge} corresponds to the interface between the active Ge particle and the inactive Li-Ge-Se coating layer.

Figs. 8a–8b show the snapshots of two order parameters, the phase-field variable (ξ) and the normalized mobile Li concentration (c_{Li}) at different lithiation times (t = 3.6s, 40s, 160s, 360s). As expected, the different degrees of $Li_{x0}Ge$ phase evolution in the particles are controlled by particle size and the mobile Li atom diffusion path. The small particles are lithiated faster than the large ones because of the smaller the radius of the particle provides the shorter the diffusion path. In each particle, the $Li_{x0}Ge$ phase evolution is inhomogeneous during the lithiation process, i.e., in the largest particle in Fig. 8a. This is because of the diffusion of the mobile Li atom in the Li-Ge-Se network. In Fig. 8b, at the early stage of lithiation, in the entire particle cluster, the mobile Li influx is not evenly distributed nor saturated in the Li-Ge-Se network. For example, at lithiation time t = 3.6s, the particles that is near the outer surface of the electrode starts lithiating, whereas

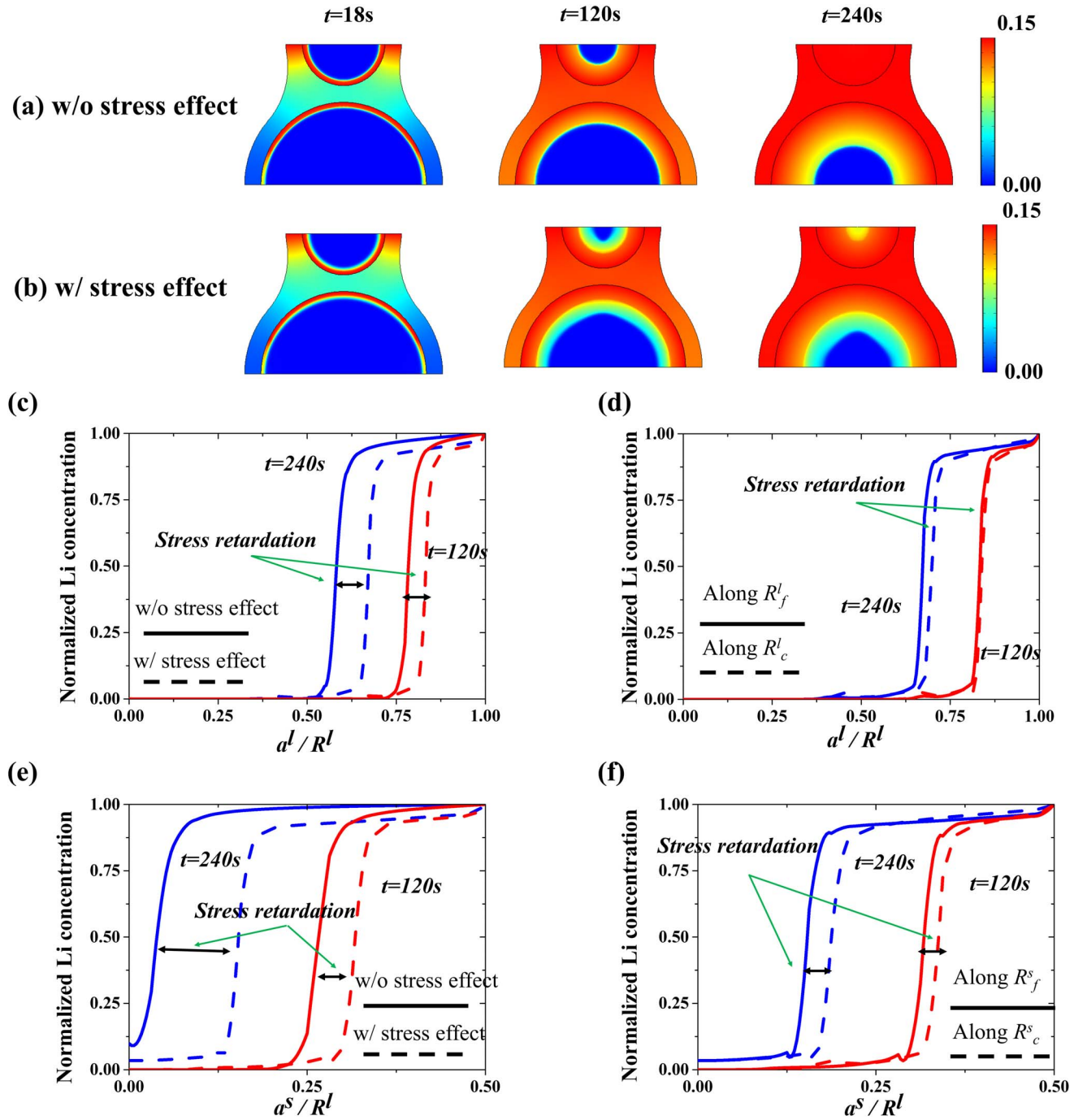

Figure 6. (a) The mobile Li distribution at different lithiation time as t = 18s, 120s and 240s in the case without stress effect. (b) The mobile Li distribution at different lithiation time as t = 18s, 120s and 240s in the case without stress effect. (c-f) Stress retardation due to the mechanical confinement of the Li-Ge-Se coating and particles contact. (c) Comparison of radial distribution of total Li along the free radius due to the stress effect in the particle of large size. (d) Comparison of total Li profiles along two radii (free radius and contact radius) of different orientations of the particle of large size. (e) Comparison of radial distribution of total Li along the free radius due to the stress effect in the particle of small size. (f) Comparison of total Li profiles along two radii (free radius and contact radius) of different orientations of the particle of small size.

the particles inside of the electrode remain in pristine state. As Fig. 8b shows, it takes about 40s for the Li-Ge-Se network to reach a saturated and evenly distributed state of the mobile Li. Before that, the mobile Li distribution in the Li-Ge-Se layer is inhomogeneous, causing an inhomogeneous lithiation of the particles, and, therefore, resulting in uneven mean stress distribution in the radial direction in each particle, given in Fig. 8c. Also, the mechanical constraint of the Li-Ge-Se network results in a high compressive mean stress at the center of the particles that are fully lithiated. This is because, the volume expansion of the particles leads to tensile stress at the surface of the particle during the final stage of lithiation. To balance the particles' surface tensile stress, a high compressive stress at the center of particle and a tensile stress in the Li-Ge-Se network are required. However, the large particles continue swelling, hence increase the tensile stress in the Li-Ge-Se network. Therefore, the tension is balanced by the large compressive stress inside the lithiated particles. This compressive mean stress impedes Li insertion into the particles, reducing the electrode effective capacity.

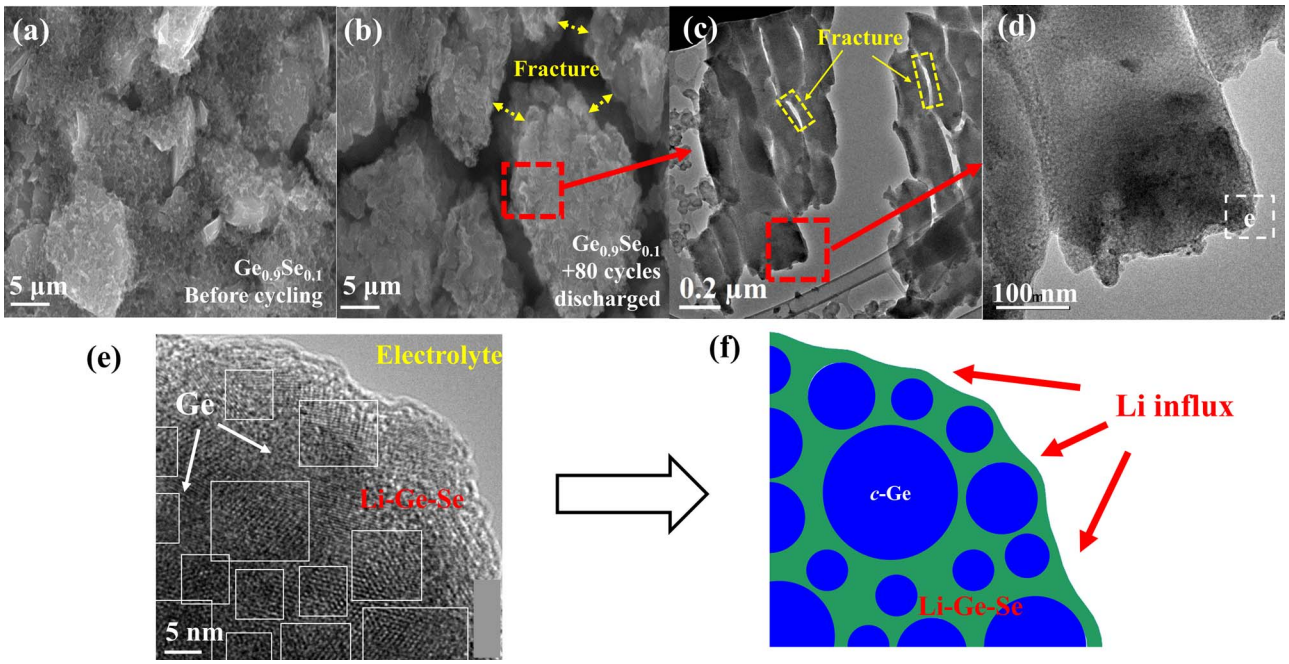

Figure 7. (a) Experimental SEM image of Se-doped Ge ($Ge_{0.9}Se_{0.1}$) electrode particles before cycling. (b) SEM image of the of $Ge_{0.9}Se_{0.1}$ electrode particles after cycling. (c-e) HR-TEM images of the active material, Ge particle (crystal zone), surrounded by amorphous Li–Ge–Se phase (light region). (f) Schematic diagram of the representative element of a $Ge_{0.9}Se_{0.1}$ electrode particle. *c*-Ge (blue) and network of Li-Ge-Se phase (green).

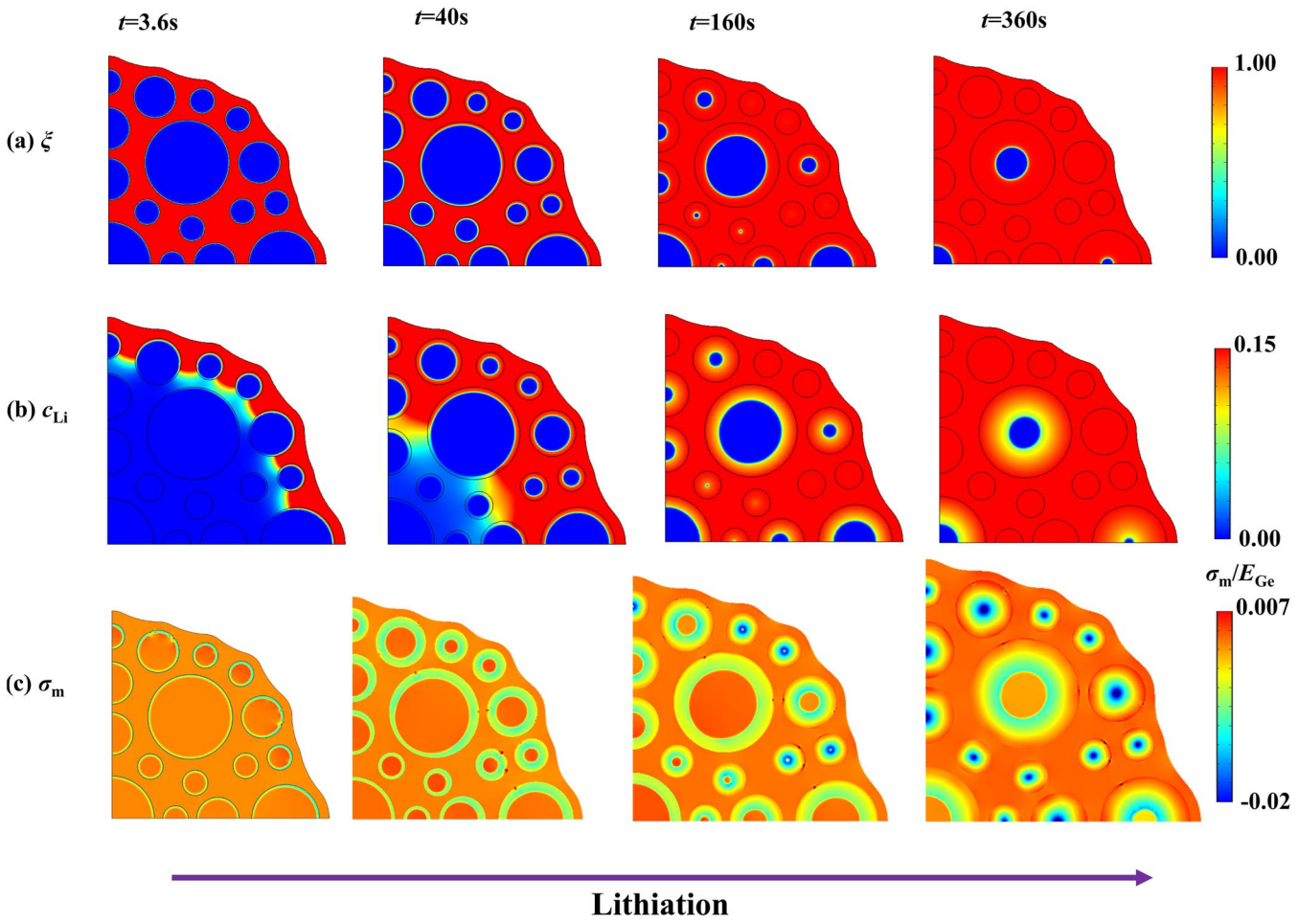

Figure 8. Evolution of (a) the phase-field ξ (b) the normalized mobile Li concentration c_{Li} and (c) the mean stress distribution at different lithiation times t = 3.6s, 40s, 160s, 360s.

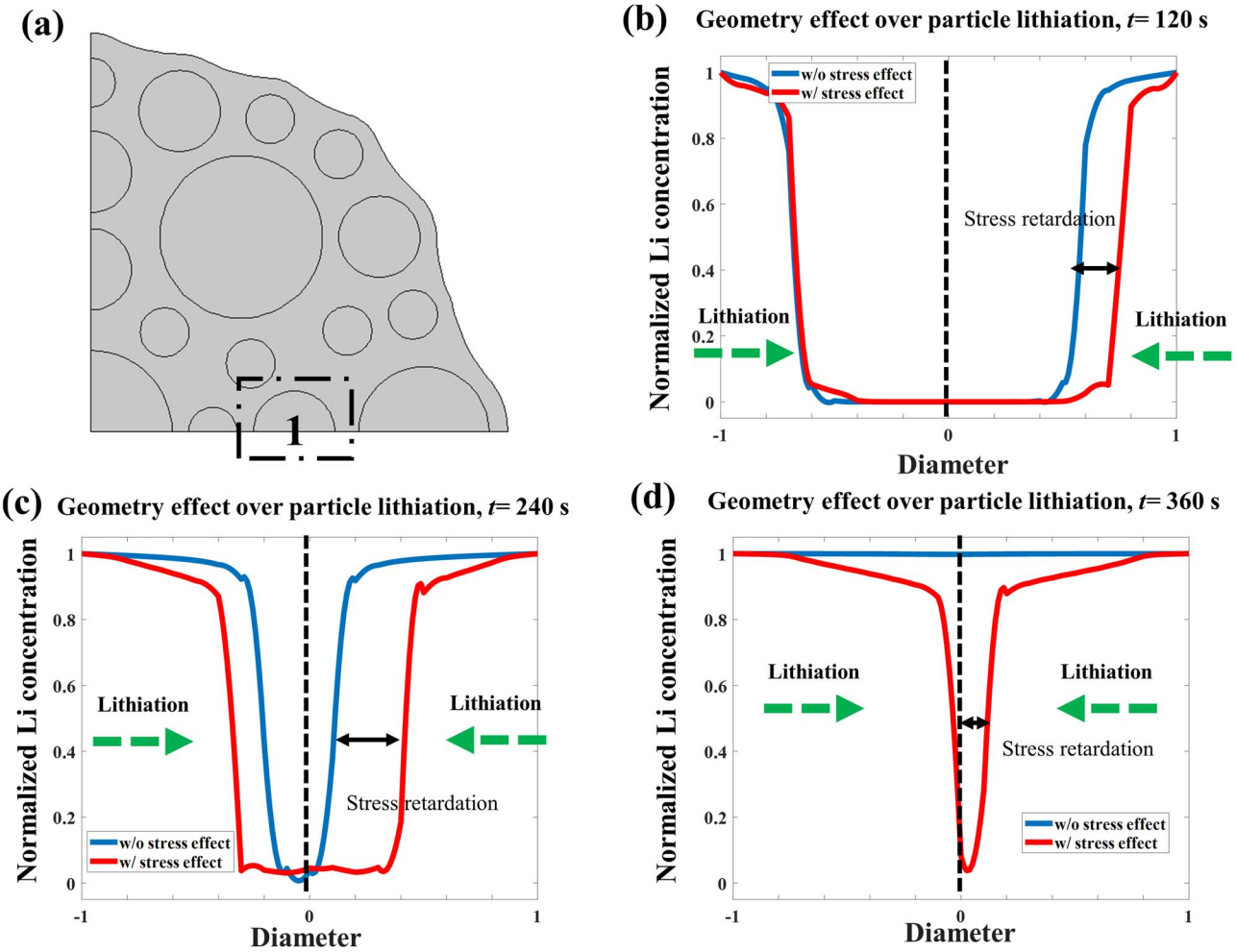

Figure 9. Comparison of total Li distribution in (a) the particle "1" at different lithiation time, as (b) $t = 120$ s, (c) 240 s, and (d) 360 s.

For further analysis of self-limiting phenomena caused by the lithiation induced stress, we choose particle "1" for illustration, identified in Fig. 9a. The particle is located between a larger particle (right) and a smaller one (left). The green solid line represents the axis of the chosen particle, the other solid lines represent the Li distribution without stress effect, and the dash line accounts for the stress effect. Figs. 9b–9d shows the uneven lithiation in the chosen particle "1", at time (b) $t = 120$s, (c) $t = 240$s and (d) $t = 360$s, respectively. The Li distribution across the diameter of the particle is axisymmetric, corresponding to a faster lithiation at the right side of the particle (as also shown Fig. 8b). When the stress effect is considered, a large compressive mean stress concentrates at the center of the particle, impeding Li insertion into the particle. For example, at $t = 360$ s, when the stress effect is ignored, the particle is saturated with Li (blue solid line), but by considering the stress effect, the Li concentration at the center of the particle is much lower (blue dash line). Third, more lithiation retardation is experienced at the right side of particle "1" when the stress effect is considered, as shown in Figs. 9b–9d. The right side of the particle has lower Li concentration than the left side. This is because the large particle at the right side of "1" exerts more stress at that region than the stress exerted on "1" by the smaller particle at the left. This result indicates that smaller particles are more affected by adjacent particles resulting in the generation of large compressive stress in the center during lithiation.

Avoiding structure disintegration, i.e., the fracture in the Li-Ge-Se phase and interfacial debonding between the active *c*-Ge particle and the Li-Ge-Se network is very important in the optimization of the electrochemical performance of electrodes. We analysis the stresses in the structure to understand the failure risk. Figs. 10a and 10b show the maximum tensile stress and shear stress in the Li-Ge-Se network, respectively. The maximum normal stress is located at the region surrounding the active particles, especially at the outer surface of the electrode. The maximum shear stresses are between the neighboring particles, especially between the large and small particles. It shows that a large size difference between adjacent particles generates higher shear stress. The normal stress could result in irreversible morphology changes or fracture of the Li-Ge-Se network, which could reduce the mobile Li transportation path for the particle leading to an uneven lithiation and capacity loss. The shear stress is the driving stress

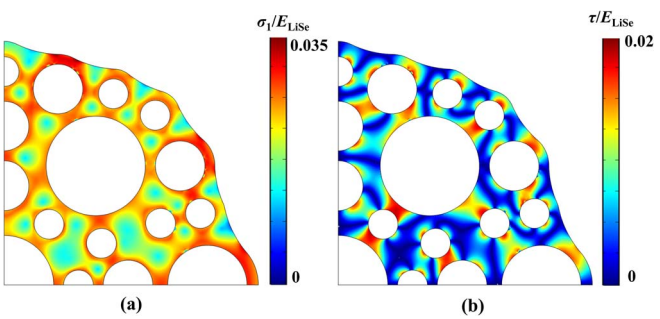

Figure 10. Contours of (a) the maximum tensile stress and (b) the shear stress in the Li-Ge-Se network.

for interfacial debonding between the particles and the network. A debonded interface could isolate the active particles and increase the ohmic and thermal resistance of the electrodes—another known factor that causes persistent capacity loss of the electrodes over cycles.

Conclusions

The mechanical stresses and electrochemical behaviors of Li-ion batteries are intimately coupled. Motivated by the experimentally observed network of active/inactive-phase structure in the lithiated Se-doped Ge electrode particles, in this paper, we applied a PFM coupled with elasto-plastic deformation and contact mechanics to simulate the stress and phase morphology between particles of different sizes. First, the comparison between the hypothetical contact structure and the network structure of the inactive Li-Ge-Se phase indicated that the network structure promotes even mean stress distribution near the contact area of neighboring particles. Secondly, the lithiated phase morphology and the mobile Li distribution were studied utilizing the network structure of the Li-Ge-Se phase. The result indicated a higher compressive stress at the reaction front toward the contact radial direction, impeding the mobile Li insertion into the particles. Furthermore, the small particle loss more capacity than the large one at same lithiation time due to a higher buildup of compressive stress induced by lithiation. Finally, we simulated the stress and phase evolution in a $Ge_{0.9}Se_{0.1}$ based micrometer-sized particle cluster containing multiple particles of different sizes (nanometer-sized *c*-Ge). The outcome indicated that the large compressive stress concentrated at the center of the particles after full lithiation, potentially results in results in slowing down lithiation process of particle. Also, inhomogeneous lithiation in the smaller particle is observed due to uneven mobile Li influx, inhomogeneous Li distribution at the early stage of lithiation process, and the contact influence from the larger neighboring particle. Also, we noticed that large shear stress is generated between large and small particles, indicating possible debonding or failure location. The present study potentially offers valuable insights and guidance toward designing high performing anodes with combined active/inactive-phase for Li-ion batteries.

Acknowledgment

This work is financially supported by NSF under CBET-1604104 and CBET-1603491. Dr. C. B. Mullins also gratefully acknowledges the generous support of the Welch Foundation via grant F-1436. The computer simulations were carried out on the clusters of High Performance Computing Collaboratory (HPC^2) at Mississippi State University.

Appendix

Phase-field model.—To simulate the concurrent Li diffusion and chemical reaction, two phase-field parameters will be defined corresponding to the states of Li during the lithiation process: 1) we define the mobile Li (as unreacted Li atoms) distribution in the phases via the normalized concentration field (molar fraction), $c_{\mathrm{Li}} = x/x_{\max}$, where x is the number of moles of the mobile Li, and $x_{\max} = 4.4$ is the maximum number of moles of total Li.[83] 2) a continuous phase-field variable, ξ, is introduced to describe the immobilized Li state (reacted Li), and applied to separate *a*-$Li_{x0}Ge$ and *c*-Ge during the phase transformation. This order parameter varies smoothly across the interface with $\xi = 0$ in the *c*-Ge phase (unlithiated state) and $\xi = 1$ in the *a*-$Li_{x0}Ge$ phase (lithiated state). Besides, trapping Li and forming *a*-$Li_{x0}Ge$ phase are the same process in the electrode during lithiation, so we can simply find out a relationship between the phase variable ξ and the normalized concentration of immobilized Li as $c_{\mathrm{Li}}^{\mathrm{Trapped}} = (x_0/x_{\max}) \cdot \xi = (3.75/4.4) \cdot \xi = 0.85\xi$.

With above two phase-field parameters, we define the total free energy functional of the heterogeneous material expressed as[45,67,68]

$$G = \int_V f dV = \int_V \left[f_{ch}(\xi) + f_{mobile}(c_{\mathrm{Li}}) + \frac{\kappa_\xi (\nabla \xi)^2}{2} + \frac{\kappa_c (\nabla c_{\mathrm{Li}})^2}{2} + f_\sigma(\mathbf{F}, \xi, c_{\mathrm{Li}}) \right] dV \quad [A1]$$

where the terms $\kappa_\xi(\nabla\xi)^2/2$ and $\kappa_c(\nabla c_{Li})^2/2$ are the gradient energy densities associated with the interfacial energy.

(i) $f_{ch}(\xi)$ corresponds to the local chemical free energy density, reads

$$f_{ch}(\xi) = g(\xi) + h(\xi)\eta \quad [A2]$$

(ii) $f_{mobile}(c_{\mathrm{Li}})$ is the free energy density of the mobile Li interacting with host matrices, expressed as

$$f_{mobile}(c_{\mathrm{Li}}) = x_{\max}\left\{\mu_{Li}^0 c_{\mathrm{Li}} + RT\left[c_{\mathrm{Li}} ln(c_{\mathrm{Li}}) + (1 - c_{\mathrm{Li}}) \ln(1 - c_{\mathrm{Li}})\right] + \Omega c_{\mathrm{Li}}(1 - c_{\mathrm{Li}})\right\} \quad [A3]$$

where μ_{Li}^0 is the chemical potential of a mobile Li atom not interacting with the host matrices, the dimensionless parameter Ω describes the energy interaction between the mobile Li atoms and empty intercalation sites. T is the temperature, R is the gas constant. Then, we obtain the potential for the mobile Li in stress-free state as $\mu_{mobile}^{\mathrm{c}} = \frac{\partial f_{mobile}}{\partial c_{\mathrm{Li}}} = x_{\max}[\mu_{Li}^0 + RT(\mathrm{In}\frac{c_{\mathrm{Li}}}{1-c_{\mathrm{Li}}}) + \Omega(1 - 2c_{\mathrm{Li}})]$.

(iii) $f_\sigma(\mathbf{F}, \xi, c_{\mathrm{Li}})$ is the elastic energy density induced by the inhomogeneous lithiation, which is related to the stress states of the phases across the reaction front. In this study, the elastic energy density is defined as $f_\sigma(\mathbf{F}, \xi, c_{\mathrm{Li}}) = \frac{J^e E}{2(1+\nu)}(tr(\mathbf{E}^e\mathbf{E}^e) + \frac{\nu}{1-2\nu}[\mathrm{tr}(\mathbf{E}^e)]^2)$ in the Lagrangian description (initial configuration) by following our previous work.[67] Hence, we express the stress driving force in two folds, μ_σ^ξ and μ_σ^c, corresponding to the resulting stresses caused by the immobilized Li and the mobile Li, respectively, as[84]

$$\begin{cases} \mu_\sigma^\xi = \frac{\partial f_\sigma(\mathbf{F},\xi,c_{\mathrm{Li}})}{\partial \xi} = \beta_1 \sigma_m + \frac{1}{2}\frac{\partial C_{ijkl}}{\partial \xi} E_{ij}^e E_{kl}^e \\ \mu_\sigma^c = \frac{\partial f_\sigma(\mathbf{F},\xi,c_{\mathrm{Li}})}{\partial c_{\mathrm{Li}}} = \beta_2 \sigma_m + \frac{1}{2}\frac{\partial C_{ijkl}}{\partial c_{\mathrm{Li}}} E_{ij}^e E_{kl}^e \end{cases} . \quad [A4]$$

where σ_m is the mean stress induced by the lithiation. And the terms $(1/2)(\partial C_{ijkl}/\partial\xi)E_{ij}^e E_{kl}^e$ and $(1/2)(\partial C_{ijkl}/\partial c_{\mathrm{Li}})E_{ij}^e E_{kl}^e$ describe the driving forces from the varying elastic modulus of the material during lithiation, in which C_{ijkl} is the component of the fourth-rank tensor of elastic moduli $\mathbf{C}$. Moreover, when the mobile Li starts to be trapped in Li-Ge alloy, the value of elastic properties of the active lithiated Ge material vary between the pure Ge and $Li_{3.75}Ge$'s properties.[16] Hence, $\mathbf{C}$ is obtained as, $\mathbf{C}(\xi) = 2\lambda(\xi)\mathbf{I} + (K(\xi) - (2/3)\lambda(\xi))\ \mathbf{1} \otimes \mathbf{1}$, in which bulk modulus $K(\xi) = E_{\mathrm{eff}}/(3(1-2\nu_{\mathrm{eff}}))$ and shear modulus $\lambda(\xi) = E_{\mathrm{eff}}/(2(1+\nu_{\mathrm{eff}}))$. ν_{eff} is the effective Poisson's ratio and the effective Young's modulus E_{eff} is interpolated by $E_{\mathrm{eff}} = E_{\mathrm{LiGe}}\ h(\xi) + (1 - h(\xi))\ E_{\mathrm{Ge}}$, in which E_{LiGe} is the Young's modulus of $Li_{3.75}Ge$ and E_{Ge} is the Young's modulus of pure Ge, respectively.

Note that the plastic energy density is ignored based on the assumption of which is independent of the concentration of Li atom[67,72] but only related to the deformation gradient $\mathbf{F}$. Because the plastic deformation is an irreversible process and does not contribute to the free energy or chemical potential.[48] Hence, the plastic energy density has no contribution to the driving force of lithiation process (neither the phase evolution nor the mobile Li diffusion).

The reaction is expected to consume the Li that is in a mobile state, thus, the increase of ξ is accompanied with a decrease of mobile Li concentration, i.e., c_{Li}. Based on the mass conservation law, we define the mobile Li diffusion in the host matrices as

$$\frac{\partial c_{\mathrm{Li}}}{\partial t} = -\nabla \cdot \mathbf{j}_{\mathrm{Li}} - \frac{x_0}{x_{\max}}\frac{\partial \xi}{\partial t} \quad [A5]$$

where the last term $\frac{x_0}{x_{\max}}\frac{\partial \xi}{\partial t}$ responses to the accumulation/consuming of the mobile Li due to lithiation reaction. And $\mathbf{j}_{\mathrm{Li}}$ is the mobile Li concentration influx, which is obtained by the conventional expression as,[67]

$$\mathbf{j}_{Li} = -M_{\mathrm{Li}}\nabla\frac{\delta G}{\delta c_{Li}} = -M_{\mathrm{Li}}\nabla\mu_{\mathrm{Li}}^{\mathrm{c}} \quad [A6]$$

where $M_{\mathrm{Li}} = D_{\mathrm{Li}}^{\mathrm{eff}} c_{\mathrm{Li}}(1 - c_{\mathrm{Li}})/x_{\max} RT$ is the mobile Li mobility tensor that is in general a function of the mobile Li concentration.[67] And the total mobile Li potential, $\mu_{\mathrm{Li}}^{\mathrm{c}}$, is related to the mobile Li concentration, and the local stress state, as

$$\mu_{\mathrm{Li}}^{\mathrm{c}} = \frac{\delta G}{\delta c_{Li}} = \mu_{mobile}^{\mathrm{c}} + \kappa_c\nabla^2 c_{\mathrm{Li}} + \mu_\sigma^c = x_{\max}\left[\mu_{Li}^0 + RT\left(\mathrm{In}\frac{c_{\mathrm{Li}}}{1 - c_{\mathrm{Li}}}\right) + \Omega(1 - 2c_{\mathrm{Li}})\right] + \kappa_c\nabla^2 c_{\mathrm{Li}} + \mu_\sigma^c \quad [A7]$$

if ignoring the stress effect on the diffusion driving force, reducing the number of material constants and excluding from the consideration of some secondary important phenomena, we adopt an alternative simpler approach for $\mathbf{j}_{\mathrm{Li}}$, as

$$\mathbf{j}_{\mathrm{Li}} = -D_{\mathrm{Li}}^{\mathrm{eff}}\nabla c_{\mathrm{Li}} \quad [A8]$$

where $D_{\mathrm{Li}}^{\mathrm{eff}}$ is the effective diffusion coefficient in the active lithiated Ge material interpolated by $D_{\mathrm{Li}}^{\mathrm{eff}} = D_{\mathrm{Li}}^{\mathrm{LiGe}} h(\xi) + D_{\mathrm{Li}}^{\mathrm{Ge}}(1 - h(\xi))$, where $D_{\mathrm{Li}}^{\mathrm{LiGe}}$ and $D_{\mathrm{Li}}^{\mathrm{Ge}}$ are the mobile Li diffusion coefficients in the lithiated Ge and unlithiated Ge respectively. Additionally, the effective diffusion coefficient in the inactive Li-Ge-Se layer is directly set as the corresponding value, i.e. $D_{\mathrm{Li}}^{\mathrm{eff}} = D_{\mathrm{Li}}^{\mathrm{LiSe}}$.

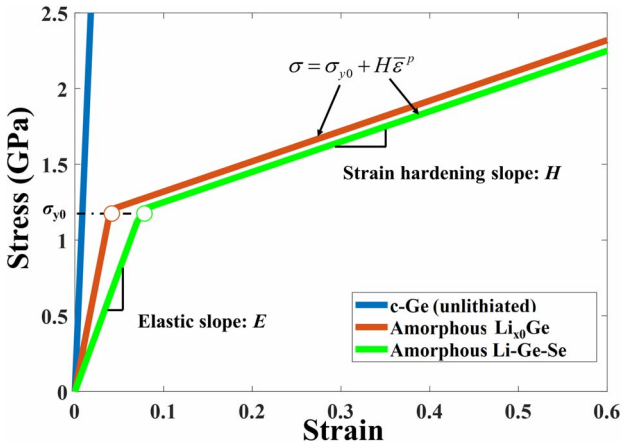

Figure A1. The stress-strain curves for the unlithited phase-pure Ge (blue) and the amorphous phases: $Li_{x0}Ge$ (red) and Li-Ge-Se (green), respectively.

Elasto-plastic deformation.—Assuming lithiation-induced chemical deformation rate is dilational without spin, the total stretch rate tensor $\mathbf{D}$ becomes the total deformation rate, and can be decomposed into three additive parts in the finite-strain plasticity framework, $\mathbf{D} = \mathbf{D}^e + \mathbf{D}^p + \mathbf{D}^c$, where $\mathbf{D}^e$, $\mathbf{D}^p$ and $\mathbf{D}^c$ are the elastic, plastic and chemical stretch rates, respectively.[85] At a general state of charge, the phase boundary separates the electrode materials into unlithiated and lithiated domains. The unlithiated domain is modeled as an elastic material, whose stress and strain rates obey the classical Hooke's law with two material constants, Young's modulus E_{Ge} and Poisson's ratio ν_{Ge}, assuming the material is isotropic. For the lithiated amorphous Li-Ge-Se and $Li_{x0}Ge$, the isotropic elasto-plastic model is adopted to describe its constitutive response, which specifies the relations between the stresses and the elastic and plastic parts of the deformation gradient. The equations are usually written in rate form, in which the stretch and stress rates are related by the following form $\tau^{\nabla e} = \frac{E_{\text{eff}}}{1+\nu_{\text{eff}}}[\mathbf{D}^e + \frac{\nu_{\text{eff}}}{1-2\nu_{\text{eff}}}\text{tr}(\mathbf{D}^e)\mathbf{I}]$, in which "tr" denotes the trace of a tensor, $\boldsymbol{\tau}$ is the Kirchhoff stress tensor that is related to the Cauchy stress tensor as $\boldsymbol{\tau} = J\boldsymbol{\sigma}$, where J corresponds to the elastic volume expansion. The superscripts in $\boldsymbol{\tau}^{\nabla e}$ denotes the Jaumann rate of $\boldsymbol{\tau}$, for which the elastic spin is involved. Different from the unlithiated domain for which the elastic constants are fixed values, the two elastic constants, Young's modulus E_{eff} and Poisson's ratio ν_{eff}, for the lithiated product (Li-Ge-Se and $Li_{x0}Ge$) are phase and Li concentration dependent, as detailed in Parameters Section.

The plastic stretch rate, $\mathbf{D}^p$, obeys the associated J_2-flow rule. Namely, plastic yielding occurs when the equivalent stress, $\tau_e = \sqrt{\frac{3}{2}\boldsymbol{\tau}' : \boldsymbol{\tau}'}$, reaches the yield strength, σ_y. Here $\boldsymbol{\tau}'$ is the deviatoric part of $\boldsymbol{\tau}$, i.e., $\boldsymbol{\tau}' = \boldsymbol{\tau} - tr(\boldsymbol{\tau})\mathbf{I}/3$. According to J_2-flow theory, the plastic stretch rate is given by $\mathbf{D}^p = \frac{3}{2}\frac{\boldsymbol{\tau}'}{\tau_e}d^p_{eq}$, where $d^p_{eq} = \sqrt{2\mathbf{D}^p : \mathbf{D}^p/3}$ is the equivalent plastic stretch rate.

The lithiated electrode and Li-Ge-Se phase are modeled as isotropic elasto-plastic materials with a simple linear hardening rule $\sigma_y = \sigma_{y0} + H\bar{\varepsilon}^p$, where σ_{y0} denotes the initial yield strength, H is the hardening modulus of the material, and $\bar{\varepsilon}^p$ is the total accumulated equivalent plastic stretch, given by: $\bar{\varepsilon}^p = \int_t d^p_{eq}\,\mathrm{d}t$.

Fig. A1 shows the simple stress-strain curves for solid phases. Since the unlihitaed domain (c-Ge) is modeled as an elastic material, the stress-strain curve of c-Ge is a straight line (blue) with the slope of 130 GPa (E_{Ge}). Both of the amorphous phases are treated as isotropic elasto-plastic materials with a simple linear hardening rule. The stress-strain curves for $Li_{x0}Ge$ (red) and Li-Ge-Se are consisted by two portions, as elastic and plastic, respectively. For the elastic portion, the elastic slopes are 30 GPa ($E_{\text{Li-Ge}}$ for $Li_{x0}Ge$ phase) and 16 GPa ($E_{\text{Li-Ge-Se}}$ for Li-Ge-Se phase). For the plastic portion, however, the materials properties of amorphous Li-Ge-Se and $Li_{x0}Ge$ in the plastic region are unavailable. Hereby, we use typical values for the yield strength $\sigma_{y0} = 1.2$ GPa, and the hardening modulus $H = 2.0$ GPa, which provide a reasonable fit to recent experiments,[42] as mentioned in Parameters Section.

Lithiation process in Ge particles enveloped by an inactive Li-Ge-Se network.—Different from the pure c-Ge electrode particles, the active c-Ge nanoparticles in the Se-doped Ge particles is enveloped by an inactive amorphous Li-Ge-Se layer which is not involved in the reaction. As shown in Figs. A2a and A2b, a salient feature of lithiation is the formation of a sharp phase boundary in the crystalline Ge electrode, which separates the Li-rich phase (a-$Li_{x0}Ge$) and Li-poor phase (c-Ge), as lithiation proceeds as shown in Fig. A2. In particular, three kinetic processes in series are included in the lithiation that are (i) the redox reaction (a charge transfer reaction) at the electrolyte/Li-Ge-Se interface, (ii) the diffusion of the mobile Li atom through the Li-Ge-Se layer and the a-$Li_{x0}Ge$ phase, and (iii) the chemical reaction (a bulk reaction) at the a-$Li_{x0}Ge$/c-Ge interface where the mobile Li is changed to the immobilized status.

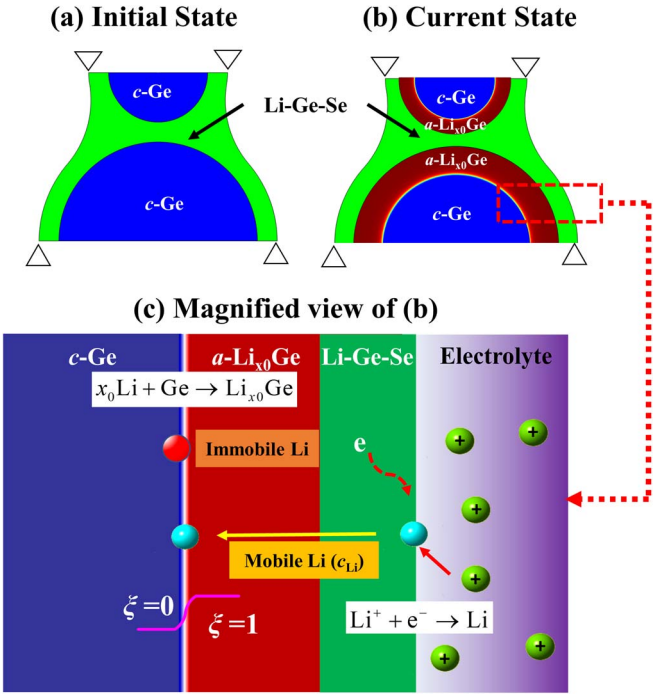

Figure A2. Schematic diagram showing a typical lithiation process from (a) the initial state with a lithiation-free and stress-free Ge/$Li_{x0}Ge$ electrode particle to (b) the current state in which the active Ge particle is partially lithiated with the sharp phase boundary, and the inactive amorphous Li-Ge-Se layer is not involved in the reaction. In particular, the lithiation arises from three kinetic processes in series that are (i) the redox reaction (a charge transfer reaction) at the electrolyte/Li-Ge-Se interface, (ii) the diffusion of the mobile Li through the inactive Li-Ge-Se and a-$Li_{x0}Ge$, and (iii) the chemical reaction (a bulk reaction) at the a-$Li_{x0}Ge$/c-Ge interface where the mobile Li is changed to the immobilized status as schematically shown in (c).

Stress effect vs. ratio of radii.—During lithiation, a small particle next to a large one can be overwhelmed by the stress field of large particle due to the dissimilarity in particle size. As a result, we find more deleterious mechanical effect, i.e., stress retardation effect, in the small particle. The key of stress retardation during particle's lithiation is the compressive mean stress at reaction front, which donates a negative stress driving force, μ^{ξ}_{σ}, in phase evolution, as shown in Eq. A4.

Hence, in this section, we run a couple of cases to show the relationship between the ratio of radii of the adjacent particles and the compressive mean stress variation along the contact radial direction. Fig. A3 compares the mechanical influence of different ratios of radii along the contact direction based on the same model used in Section Particle-particle interaction between two neighboring nanometer sized particles. First, we fix the radius of large particle (L) and increase the size of the small one (S), as S/L = 0.2, 0.5, 0.6, 0.8. The mean stress, σ_m, at the reaction front is barely impacted as the radius of smaller particle increases at the time t = 120s and 220s, given in Fig. A3a and Fig. A3b, respectively. There is a slight mechanical influence on the mean stress variation in the large particle along contact direction, but stress levels of the compressive mean stress at reaction front are barely impacted as S/L increases.

However, this is not the case when we fix the radius of the small particle (S) and increase the size of the large one (L), as L/S = 1.6, 2.0, 2.4, 2.8. In Fig. A3c and Fig. A3d, we observed an increased compressive mean stress, σ_m, at the reaction front due to L/S increase. This means that the compressive mean stress at the reaction front of small particle is proportion to the size nearby large particle.

The large particles have higher levels of lithiation-induced-stress. However, this high level of compressive stress needs a corresponding tensile stress for balance. Hence, a higher tension (or a less compressive stress) at the surface of the large particle is necessary to balance a higher compressive at the reaction front. However, the Li-Ge-Se layer between both particles acts like a "bridge" passing the pressure from the large particle to the small one. As shown in the Fig. 2, both adjacent surfaces will reach an equal stress state. The extra "stress" from the expansion of nearby large particle donates the deleterious mechanical effect on the smaller particle, compressing along the contact radial direction. As a result, a higher compressive stress at the reaction front of the smaller particle causes a greater stress retardation effect.

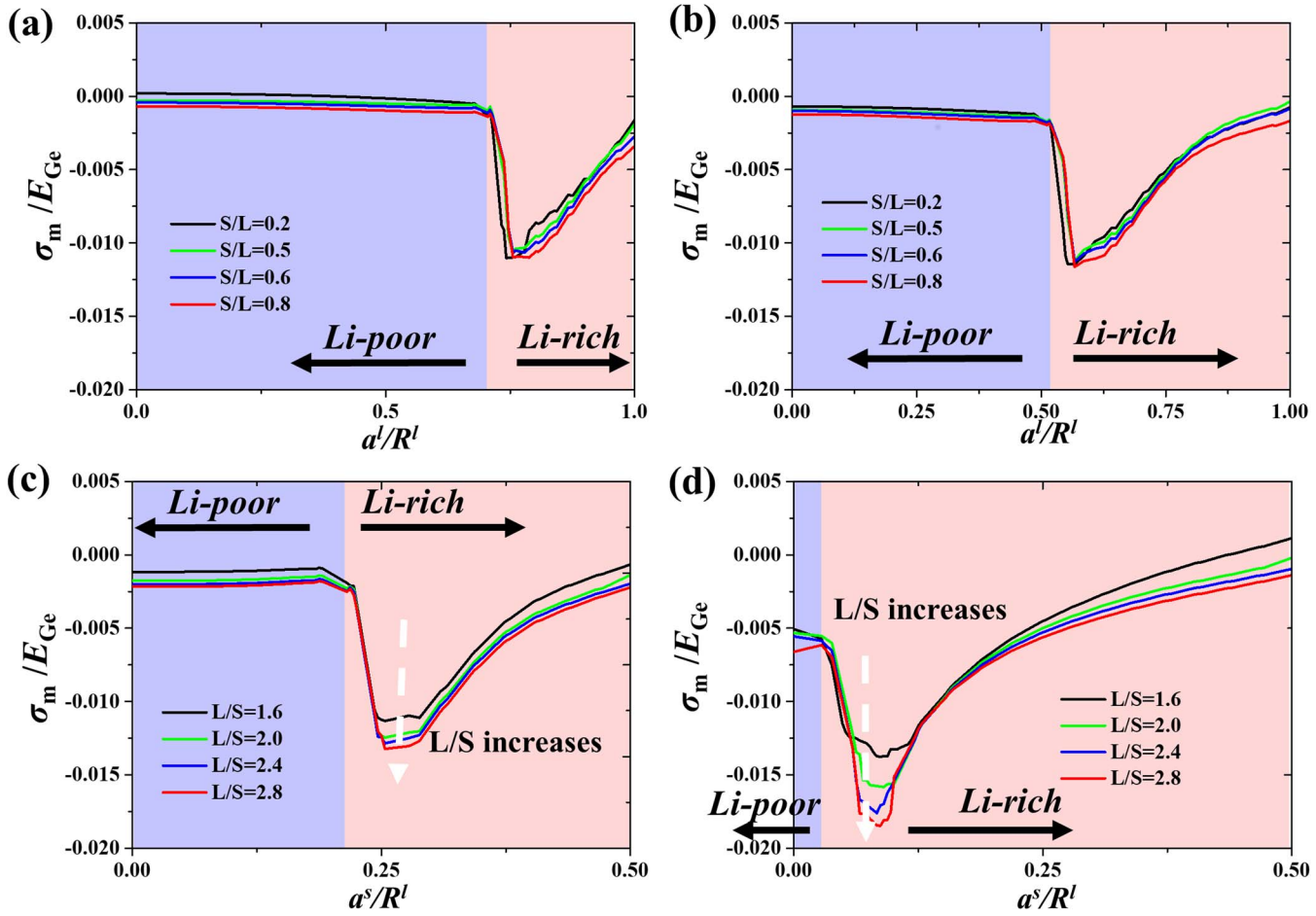

Figure A3. Comparison of particle-particle mechanical influence in different ratios of radii along contact direction. By fixing radius of large particle (L) but increasing the radius of small one (S) (i.e., S/L = 0.2, 0.5, 0.6, 0.8), (a)-(b) Contour plots showing the distribution of mean stress (σ_m) normalized by the Young's modulus of pure Ge (E_{Ge}) at different lithiation times: t = 120s and 220s. (c)-(d) By fixing radius of small particle (S) but increasing the radius of large one (L) (i.e., L/S = 1.6, 2.0, 2.4, 2.8), (a)-(b) Contour plots showing the distribution of mean stress (σ_m) normalized by the Young's modulus of pure Ge (E_{Ge}) at different lithiation times: t = 120s and 220s.

ORCID

C. Buddie Mullins https://orcid.org/0000-0003-1030-4801
L. Zhu https://orcid.org/0000-0002-6324-3718
L. Chen https://orcid.org/0000-0002-3053-7373

References

1. L. Beaulieu, K. Eberman, R. Turner, L. Krause, and J. Dahn, *Electrochemical and Solid-State Letters*, **4**, A137 (2001).
2. V. L. Chevrier, L. Liu, D. B. Le, J. Lund, B. Molla, K. Reimer, L. J. Krause, L. D. Jensen, E. Figgemeier, and K. W. Eberman, *Journal of The Electrochemical Society*, **161**, A783 (2014).
3. H. X. Dang, K. C. Klavetter, M. L. Meyerson, A. Heller, and C. B. Mullins, *Journal of Materials Chemistry A*, **3**, 13500 (2015).
4. J. Guo, A. Sun, X. Chen, C. Wang, and A. Manivannan, *Electrochimica Acta*, **56**, 3981 (2011).
5. X. Su, Q. Wu, J. Li, X. Xiao, A. Lott, W. Lu, B. W. Sheldon, and J. Wu, *Advanced Energy Materials*,**4** (2014).
6. H. Yang, X. Huang, W. Liang, A. C. Van Duin, M. Raju, and S. Zhang, *Chemical Physics Letters*, **563**, 58 (2013).
7. H. Cheng, R. Xiao, H. Bian, Z. Li, Y. Zhan, C. K. Tsang, C. Chung, Z. Lu, and Y. Y. Li, *Materials Chemistry and Physics*, **144**, 25 (2014).
8. T. Zheng and J. Dahn, in *Carbon materials for advanced technologies*, p. 341, Pergamon Amsterdam (1999).
9. W.-J. Zhang, *Journal of Power Sources*, **196**, 13 (2011).
10. M. R. Zamfir, H. T. Nguyen, E. Moyen, Y. H. Lee, and D. Pribat, *Journal of Materials Chemistry A*, **1**, 9566 (2013).
11. J. Graetz, C. C. Ahn, R. Yazami, and B. Fultz, *Journal of The Electrochemical Society*, **151**, A698 (2004).
12. X. H. Liu, S. Huang, S. T. Picraux, J. Li, T. Zhu, and J. Y. Huang, *Nano letters*, **11**, 3991 (2011).
13. M. K. Y. Chan, B. R. Long, A. A. Gewirth, and J. P. Greeley, *The Journal of Physical Chemistry Letters*, **2**, 3092 (2011).
14. W. Liang, H. Yang, F. Fan, Y. Liu, X. H. Liu, J. Y. Huang, T. Zhu, and S. Zhang, *Acs Nano*, **7**, 3427 (2013).
15. F. Shi, Z. Song, P. N. Ross, G. A. Somorjai, R. O. Ritchie, and K. Komvopoulos, *Nature communications*, **7**, 11886 (2016).
16. M. Pharr, Y. S. Choi, D. Lee, K. H. Oh, and J. J. Vlassak, *Journal of Power Sources*, **304**, 164 (2016).
17. Y. Liu, S. Zhang, and T. Zhu, *ChemElectroChem*, **1**, 706 (2014).
18. A. Mukhopadhyay and B. W. Sheldon, *Progress in Materials Science*, **63**, 58 (2014).
19. M. T. McDowell, S. Xia, and T. Zhu, *Extreme Mechanics Letters*, **9**, 480 (2016).
20. K. Zhao, M. Pharr, J. J. Vlassak, and Z. Suo, *Journal of Applied Physics*, **108**, 073517 (2010).
21. X. H. Liu, L. Zhong, S. Huang, S. X. Mao, T. Zhu, and J. Y. Huang, *Acs Nano*, **6**, 1522 (2012).
22. P. Barai, B. Huang, S. J. Dillon, and P. P. Mukherjee, *Journal of The Electrochemical Society*, **163**, A3022 (2016).
23. P. Barai and P. P. Mukherjee, *Journal of The Electrochemical Society*, **163**, A1120 (2016).
24. A. Verma and P. P. Mukherjee, *Journal of The Electrochemical Society*, **164**, A3570 (2017).
25. C. K. Chan, H. Peng, G. Liu, K. McIlwrath, X. F. Zhang, R. A. Huggins, and Y. Cui, *Nature Nanotechnology*, **3**, 31 (2008).
26. T. Kennedy, E. Mullane, H. Geaney, M. Osiak, C. O'Dwyer, and K. M. Ryan, *Nano Letters*, **14**, 716 (2014).
27. X. H. Liu, S. Huang, S. T. Picraux, J. Li, T. Zhu, and J. Y. Huang, *Nano Letters*, **11**, 3991 (2011).
28. J. Liu, Y. Li, X. Huang, R. Ding, Y. Hu, J. Jiang, and L. Liao, *Journal of Materials Chemistry*, **19**, 1859 (2009).

29. J. Y. Huang, L. Zhong, C. M. Wang, J. P. Sullivan, W. Xu, L. Q. Zhang, S. X. Mao, N. S. Hudak, X. H. Liu, A. Subramanian, H. Fan, L. Qi, A. Kushima, and J. Li, *Science*, **330**, 1515 (2010).
30. L. Chen, H. W. Zhang, L. Y. Liang, Z. Liu, Y. Qi, P. Lu, J. Chen, and L.-Q. Chen, *Journal of Power Sources*, **300**, 376 (2015).
31. A. R. Kamali and D. J. Fray, *Reviews on Advanced Materials Science*, **27**, 14 (2011).
32. J. Graetz, C. Ahn, R. Yazami, and B. Fultz, *Journal of The Electrochemical Society*, **151**, A698 (2004).
33. Q. Xiao, M. Gu, H. Yang, B. Li, C. Zhang, Y. Liu, F. Liu, F. Dai, L. Yang, and Z. Liu, *Nature communications*, **6** (2015).
34. J. Cho, *Journal of Materials Chemistry*, **20**, 4009 (2010).
35. H. Kim, B. Han, J. Choo, and J. Cho, *Angewandte Chemie*, **120**, 10305 (2008).
36. Y. Ji, L. Chen, and L.-Q. Chen, in *Thermo-Mechanical Modeling of Additive Manufacturing*, p. 93, Elsevier (2018).
37. Y. Z. Ji, Z. Wang, B. Wang, Y. Chen, T. Zhang, L. Q. Chen, X. Song, and L. Chen, *Advanced Engineering Materials*, **19**, 1600803 (2017).
38. X. H. Liu, F. Fan, H. Yang, S. Zhang, J. Y. Huang, and T. Zhu, *Acs Nano*, **7**, 1495 (2013).
39. M. Gu, H. Yang, D. E. Perea, J. G. Zhang, S. Zhang, and C. M. Wang, *Nano letters*, **14**, 4622 (2014).
40. M. T. McDowell, I. Ryu, S. W. Lee, C. Wang, W. D. Nix, and Y. Cui, *Adv Mater*, **24**, 6034 (2012).
41. P. R. Abel, M. G. Fields, A. Heller, and C. B. Mullins, *ACS applied materials & interfaces*, **6**, 15860 (2014).
42. P. R. Abel, K. C. Klavetter, A. Heller, and C. B. Mullins, *The Journal of Physical Chemistry C*, **118**, 17407 (2014).
43. K. C. Klavetter, J. P. De Souza, A. Heller, and C. B. Mullins, *Journal of Materials Chemistry A*, **3**, 5829 (2015).
44. P. R. Abel, M. G. Fields, A. Heller, and C. B. Mullins, *ACS applied materials & interfaces*, **6**, 15860 (2014).
45. X. Wang, B. Wang, M. Meyerson, C. B. Mullins, Y. Fu, L. Zhu, and L. Chen, *International Journal of Mechanical Sciences*, (2018).
46. K. Zhao, M. Pharr, L. Hartle, J. J. Vlassak, and Z. Suo, *Journal of Power Sources*, **218**, 6 (2012).
47. S. W. Lee, H.-W. Lee, I. Ryu, W. D. Nix, H. Gao, and Y. Cui, *Nature communications*, **6** (2015).
48. A. F. Bower, E. Chason, P. R. Guduru, and B. W. Sheldon, *Acta Materialia*, **98**, 229 (2015).
49. A. F. Bower, P. R. Guduru, and V. A. Sethuraman, *Journal of the Mechanics and Physics of Solids*, **59**, 804 (2011).
50. Z. Cui, F. Gao, and J. Qu, *Journal of the Mechanics and Physics of Solids*, **61**, 293 (2013).
51. H. X. Dang, K. C. Klavetter, M. L. Meyerson, A. Heller, and C. B. Mullins, *J. Mater. Chem. A*, **3**, 13500 (2015).
52. S. Huang, F. Fan, J. Li, S. Zhang, and T. Zhu, *Acta materialia*, **61**, 4354 (2013).
53. Z. Jia and W. K. Liu, *Applied Physics Letters*, **109**, 163903 (2016).
54. K. Zhao, M. Pharr, S. Cai, J. J. Vlassak, and Z. Suo, *Journal of the American Ceramic Society*, **94** (2011).
55. K. Zhao, M. Pharr, J. J. Vlassak, and Z. Suo, *Inelastic hosts as electrodes for high-capacity lithium-ion batteries*, in, AIP (2011).
56. H. Haftbaradaran, J. Song, W. Curtin, and H. Gao, *Journal of Power Sources*, **196**, 361 (2011).
57. Y. Yao, M. T. McDowell, I. Ryu, H. Wu, N. Liu, L. Hu, W. D. Nix, and Y. Cui, *Nano letters*, **11**, 2949 (2011).
58. K. Zhao, M. Pharr, J. J. Vlassak, and Z. Suo, *Journal of Applied Physics*, **109**, 016110 (2011).
59. C. Lim, B. Yan, L. Yin, and L. Zhu, *Electrochimica Acta*, **75**, 279 (2012).
60. M. T. McDowell, I. Ryu, S. W. Lee, C. Wang, W. D. Nix, and Y. Cui, *Advanced Materials*, **24**, 6034 (2012).
61. M. Gu, H. Yang, D. E. Perea, J.-G. Zhang, S. Zhang, and C. Wang, *Nano Letters*, (2014).
62. H. Wang, S. P. Nadimpalli, and V. B. Shenoy, *Extreme Mechanics Letters*, **9**, 430 (2016).
63. B. Wu and W. Lu, *Journal of Power Sources*, **360**, 360 (2017).
64. S. A. Roberts, V. E. Brunini, K. N. Long, and A. M. Grillet, *Journal of The Electrochemical Society*, **161**, F3052 (2014).
65. L. Luo, P. Zhao, H. Yang, B. Liu, J.-G. Zhang, Y. Cui, G. Yu, S. Zhang, and C.-M. Wang, *Nano letters*, **15**, 7016 (2015).
66. R. Xu and K. Zhao, *Extreme Mechanics Letters*, **8**, 13 (2016).
67. L. Chen, F. Fan, L. Hong, J. Chen, Y. Ji, S. Zhang, T. Zhu, and L. Chen, *Journal of The Electrochemical Society*, **161**, F3164 (2014).
68. L.-Q. Chen, *Annual review of materials research*, **32**, 113 (2002).
69. J. E. Guyer, W. J. Boettinger, J. A. Warren, and G. B. McFadden, *Physical Review E*, **69**, 021603 (2004).
70. J. E. Guyer, W. J. Boettinger, J. A. Warren, and G. B. McFadden, *Physical Review E*, **69**, 021604 (2004).
71. F. Gao and W. Hong, *Journal of the Mechanics and Physics of Solids*, **94**, 18 (2016).
72. A. Drozdov, *International Journal of Solids and Structures*, **51**, 690 (2014).
73. M. Roze, L. Calvez, Y. Ledemi, M. Allix, G. Matzen, and X. H. Zhang, *Journal of the American Ceramic Society*, **91**, 3566 (2008).
74. S. Kikkawa, T. Miyai, and M. Koizumi, *Solid State Ionics*, **28**, 743 (1988).
75. X.-J. Liu, L.-F. Li, and F. Lu, *arXiv preprint arXiv:1301.1745* (2013).
76. J. Wortman and R. Evans, *Journal of applied physics*, **36**, 153 (1965).
77. C. Fuller and J. Severiens, *Physical Review*, **96**, 21 (1954).
78. M. Yang, J. Zhang, H. Wei, W. Gui, H. Su, T. Jin, and L. Liu, *Scripta Materialia*, **147**, 16 (2018).
79. S. Zhang, *npj Computational Materials*, **3** (2017).
80. X. H. Liu, H. Zheng, L. Zhong, S. Huang, K. Karki, L. Q. Zhang, Y. Liu, A. Kushima, W. T. Liang, J. W. Wang, J.-H. Cho, E. Epstein, S. A. Dayeh, S. T. Picraux, T. Zhu, J. Li, J. P. Sullivan, J. Cumings, C. Wang, S. X. Mao, Z. Z. Ye, S. Zhang, and J. Y. Huang, *Nano Letters*, **11**, 3312 (2011).
81. Q. Zhang, W. Zhang, W. Wan, Y. Cui, and E. Wang, *Nano letters*, **10**, 3243 (2010).
82. L. Luo, P. Zhao, H. Yang, B. Liu, J. G. Zhang, Y. Cui, G. Yu, S. Zhang, and C. M. Wang, *Nano letters*, **15**, 7016 (2015).
83. R. Yazami, *Nanomaterials for Lithium-ion batteries: Fundamentals and Applications*, Pan Stanford Publishing (2013).
84. F. Larché and J. W. Cahn, *Acta Metallurgica*, **21**, 1051 (1973).
85. A. F. Bower, *Applied mechanics of solids*, in, CRC press (2009).